Advancements in two-dimensional materials as anodes for lithium-ion batteries: Exploring composition-structure-property relationships emerging trends, and future perspective

Hina Ghulam Ali [a], Kashif Khan [b], Muhammad Bilal Hanif [c,*], Muhammad Zubair Khan [d], Iftikhar Hussain [e], Muhammad Sufyan Javed [f], Hussein A.Z. AL-bonsrulah [g,h], Michał Mosiałek [i], Maximilian Fichtner [a,*], Martin Motola [a,*]

[a] *Helmholtz-Institute Ulm - Electrochemical Energy Storage (HIU), Helmholtzstraße 11, 89081 Ulm, Germany*
[b] *School of Materials and Energy, University of Electronic Science and Technology of China, Chengdu 611731, PR China*
[c] *Department of Inorganic Chemistry, Faculty of Natural Sciences, Comenius University Bratislava, Ilkovicova 6, 842 15 Bratislava, Slovakia*
[d] *Pak-Austria Fachhochschule: Institute of Applied Sciences and Technology Mang, Haripur 22621, KPK, Pakistan*

Keywords:
Li-ion batteries
2D materials
Graphene, transition metal dichalcogenides
MXenes, molybdenum disulfide
Tungsten sulfide
And black phosphorous

A B S T R A C T

Two-dimensional materials, including graphene and its derivatives, MXenes, and transition metal dichalcogenides, have attracted significant research attention due to their unique physicochemical properties. Among the various applications of these materials, energy storage and conversion have gained particular importance in light of the ongoing energy crisis. In this review, a critical evaluation is presented, focusing on the fundamentals, recent developments, and future perspectives of two-dimensional materials as anodes in lithium-ion batteries. The emphasis of this evaluation lies specifically on the years between 2010 and 2023. The review will primarily delve into the design and manipulation of advanced interface architectures for anodes, the latest developments, and the composition structure-property relationship of transition metal dichalcogenides (TMDs), MXenes, molybdenum disulfide (MoS_2), tungsten sulfide (WS_2), and black phosphorous (BP). The main focus of the presented review revolves around modification techniques that hold great potential in energy storage applications and other energy-related fields. The exceptional characteristics of these materials, including efficient ion transport across layers and large surface areas facilitating enhanced ion adsorption and accelerated surface redox reactions, contribute to their promising performance. While we have accumulated about twenty years of experience in energy conversion applications, particularly in lithium-ion batteries, we found that a large number of articles have been published on electrodes and electrolytes. However, a critical discussion about the composition structure-property relationship, along with challenges and optimizing strategies for anodes, is still lacking. Therefore, this review aims to fill that gap. Additionally, an overview of recent research advances is provided, focusing on the application of 2D materials in advanced energy storage systems beyond conventional lithium-ion batteries. Key findings and strategies employed to address associated challenges are examined while considering the prospects of these materials in the field.

1. Introduction

Energy is an essential component for enhancing people's quality of life and achieving robust economic growth. With the global population on the rise and the emergence of an interconnected economy, the demand for energy worldwide is experiencing rapid growth. Total global

* Corresponding authors.
E-mail addresses: bilalhanif46@gmail.com, hanif1@uniba.sk (M.B. Hanif), maximilian.fichtner@kit.edu (M. Fichtner), martin.motola@uniba.sk (M. Motola).

energy consumption increased from 54,207 TWh in 1973 to 111,125 TWh in 2016. Therefore, energy storage systems play a crucial role in ensuring sustainable resilience and are of utmost importance in modern transportation and on-grid applications for the general public. These storage schemes are vital technologies for ensuring future energy flexibility and meeting the needs of people worldwide [1]. However, in the current world characterized by severe environmental challenges and energy crises, researchers are focusing on various methods of energy storage and actively promoting the development of energy storage technologies. These technologies are crucial for addressing the demands of smart cities, the Internet of Things (IoT), and other applications requiring continuous remote power supply for storage, sensing, communication, and data processing. The modern world requires the advancement of innovative energy storage systems that are cost-effective, environmentally friendly, and possess high energy density [3–5]. Electrochemical energy storage has garnered significant attention due to its remarkable efficiency and eco-friendliness. In this domain, supercapacitors have emerged as crucial devices capable of storing and delivering energy with high power density, bridging the gap between traditional capacitors and batteries. Metal-ion batteries, including lithium-ion, sodium-ion, and potassium-ion batteries, are favored for their impressive energy density and operating voltage, making them suitable for a wide array of applications such as electric vehicles, mobile phones, and supercomputers. Notably, rechargeable lithium-ion batteries (LIBs) hold immense significance in the realm of electric vehicles, portable electronics, and large-scale on-grid energy storage systems. LIBs are widely considered as the most suitable energy storage system for fulfilling the demands of practical applications [6–8].

Due to the rapid advancements in new-generation technological applications, the superior performance of portable energy devices has become essential [9]. The demand for rechargeable lithium-ion batteries (LIBs) with large energy density, long cycle life, and low cost is significantly high [10]. Achieving high-energy-density batteries involves the use of electrode materials with enhanced specific capacities compared to currently available counterparts [11]. The development of cost-effective energy storage systems is a prominent research area, particularly in the field of electrochemical energy storage for LIBs. The battery components, including anode, cathode, and electrolyte materials, play a crucial role in the overall performance of LIBs and battery systems in general. Currently, the anode is a topic of extensive discussion, and graphite is the most commonly used commercialized negative electrode material for LIBs. Graphite LIBs possess a theoretical capacity of 372 mAh g^{1}, assuming complete intercalation of LiC6 [12].

Nevertheless, due to its low specific capacity, graphite is unable to satisfy the demand for new-generation anodes. Thus, several other anode materials, such as Si, $NiCo_2O_4$, Sn, SnO_2, and S, seem promising as they exhibit considerable progressive theoretical Li^+ storage capacities. However, numerous challenging complications have been observed, such as large volume changes induced during the charge/discharge process [13], which limits their commercial applications as anodes for LIBs. These anodes face rapid capacity decline and poor cycling stability performance. In order to overcome these practical drawbacks, extensive research has been conducted to develop novel materials with high theoretical capacity, such as SnO_2, SiO_2, and Fe_3O_4 [14]. However, to this day, all of these materials suffer from severe pulverization due to volume expansion during electrochemical cycling, leading to rapid capacity decline. In order to progress in the development of new anode (and cathode) materials that possess high theoretical and experimental capacities, as well as rapid electrochemical reaction kinetics, there is a need for innovative chemistries that offer higher capacities and exceptional cycling performance. The demand for flexible anode materials is particularly high, emphasizing the importance of exploring materials that can accommodate bending and stretching without compromising their electrochemical properties [2].

The major problem with such electrode materials lies in their high cost (with enhanced activity) or relatively low cost (with decreased activity). Consequently, there is an urgent need to develop new electrode materials that offer both high efficiency and low cost. In this regard, two-dimensional (2D) materials show great promise for electrodes [15]. Graphene, as a representative 2D material, was successfully developed by Novoselov et al. in 2004 [16]. From a structural standpoint, graphene consists of a monolayer of sp^2 carbon atoms. This structural concept was hypothesized in 1947 and eventually realized in the first year of this new era [17]. According to a review published in 2007, graphene can be defined as a single sheet of graphite, an allotrope of carbon, with atoms arranged in a honeycomb framework. Nowadays, graphene is one of the most extensively studied 2D materials [18]. The synthesis of graphene was achieved through the micromechanical cleavage of graphite using Scotch tape in 2004 [19]. Since then, researchers have devoted significant attention to the field of 2D materials, with graphene being studied extensively. Graphene's popularity arises from its wide array of appealing properties, which are a result of its remarkable electronic properties. These properties include a zero bandgap, extremely high electrical conductivity (up to * 106 S cm^{1}), exceptional thermal conductivity, large carrier RT intrinsic mobility (up to * 200,000 cm^2 (Vs) ^{1}), high mechanical strength (with a Young's modulus of * 1 TPa), an astonishingly high theoretical specific surface area (2630 m^2/g), outstanding optical properties, and excellent morphological structures. Graphene's distinct properties have enabled its application in various fields such as energy, catalysis, optoelectronics, and biomedicine. Nonetheless, despite its favorable attributes, graphene does possess limitations. The absence of band gaps and its relatively low light absorption capacity are particularly significant drawbacks, especially when considering their importance in modern electronic devices.

However, these limitations can be overcome through the implementation of appropriate measures, such as chemical functionalization. In general, 2D materials exhibit unique physicochemical properties that make them suitable for a wide range of applications. They possess inherent conductivity, enabling them to be used for chemical modification and electron transfer. They also show great potential for flexible device applications. Additionally, they exhibit reversible redox reactions that contribute to high capacity retention, fast ion-diffusion kinetics for excellent rate performance, and host materials that provide additional active sites for increased specific capacity and electrocatalytic functions. Moreover, their large specific surface area promotes ion adsorption and enhances capacitance, while their interlayer structure can be tuned. Collectively, these advantages position 2D materials as promising candidates for energy storage applications [18,19]. However, there is still ample room for improvement in 2D materials, such as achieving a direct band gap (which is currently under development). Furthermore, the expandability of 2D materials is a distinct advantage, as their structures and properties can be easily adjusted and controlled by modifying the surface atoms. These unique characteristics have led to widespread anticipation and applications of 2D materials, particularly in areas such as photoelectric devices, electrocatalysis, electrochemical energy storage devices, batteries, supercapacitors, solar cell electrodes, solar cells, and sensors. Over the past few decades, 2D materials have also made significant advancements in new-generation transistors, photoemitting devices, hydrogen storage, catalysis, lubricants, anti-corrosion applications, and photonics [20–23].

2. Unleashing the power of 2D materials: a paradigm shift in lithium-ion battery anodes

Following the footsteps of graphene, numerous categories of 2D materials have been derived. One such category is the mono-elemental analogues of graphene (MEAs), which include graphene and its derivatives such as graphene oxide and reduced graphene oxide. Additionally, there are other forms of elemental analogues of graphene, such as germanene, silicene, borophene, phosphorene, and stanene. Transition metal oxides (TMOs) like V_2O_5 [24], MoO_5 [25], Mn_3O_4 [26], and

MnO_2 [27], as well as transition-metal chalcogenides (TMCs) and transition metal dichalcogenides (TMDs), are also examples of 2D materials that have been explored. Among the various 2D materials, transition metal dichalcogenides (TMDs) have garnered significant attention. TMDs exhibit the MX2 configuration, where M denotes a transition metal atom (such as Nb, Mo, V, or W) and X represents a chalcogen atom (such as Te, S, or Se). Currently, popular TMDs include TiS_2 [28], VS_4 [29], VS_2 [30], WSe_2 [31], $Ni_{0.75}Fe_{0.25}Se_2$ [32], MoS_2 [33], and heterostructured $CoSe_2$/ZnSe [34]. Another noteworthy category within the TMDs family is MXenes, which encompass transition metal carbides, nitrides, and carbonitrides. MXenes, such as Ti_3C_2Tx [35], V_2CT_x [36], Ti_2CT_x [37], and $Nb_4C_3T_x$ [38], alongside other 2D structures like hBN, represent emerging and relatively new 2D materials. Notably, both graphene and 2D TMDs possess a direct bandgap. 2D TMDs possess promising applications in high-end electronics, spintronics, optoelectronics, and energy storage and conversion, owing to their strong spin-orbit synergy and favorable electronic and mechanical properties [39].

Scientists have devoted significant attention to the discovery of new inorganic 2D materials. Through first-principles calculations, single-layer III-V materials [40] and 2D group IV mono-chalcogenides have emerged as promising candidates among the newly identified 2D materials [41]. Additionally, certain TMDs like SiGe and SiS_2 have been proposed for their potential applications in electronic and optoelectronic devices [42]. However, further research is needed to explore the existence of these potential 2D structures and other yet unknown 2D materials. Fig. 1 illustrates the major classes of 2D materials.

2D materials exhibit a wide range of geometries and structures. Mono-elemental analogues of graphene (MEAs) are considered as distinct 2D materials that consist of a single element and possess structures similar to graphene. Currently, various MEAs materials, including silicene, phosphorene, germanene, stanene, arsenene, and antimonene, have gained significant attention. Fig. 2(a–i) provides an overview of the typical structures of common 2D materials. Additionally, in Fig. 2(j), the number of published papers on graphene oxide, MoS_2, WS_2, and phosphorene is shown, highlighting the tremendous interest in these materials.

3. Innovative synthesis approaches for 2D materials in lithium-ion battery anodes

The synthesis methods utilized for 2D materials play a crucial role as they directly impact the material's final properties, including its morphology, mechanical, chemical, and electronic properties, as well as the overall structural stability. Numerous studies have focused on the fabrication methods of 2D materials, with the most popular techniques summarized in references [44–46]. Generally, two broad approaches, known as top-down and bottom-up techniques, have been employed for the preparation of 2D materials. "Top-down" methods involve the removal of material from a bulk 3D precursor to achieve the desired layered morphology. On the other hand, "bottom-up" methods are employed to produce thin films and layers at the atomic level [46].

Technique top-down methods; include exfoliation, including mechanical exfoliation, intercalation exfoliation, and etching exfoliation.

Technique bottom-up methods; comprise chemical vapor deposition (CVD) and epitaxial growth, atomic layer deposition (ALD).

Among the various synthesis methods, exfoliation is regarded as one of the most promising techniques for obtaining 2D materials and is frequently employed in their synthesis nowadays. The fundamental principle of exfoliation involves reducing the interaction between different layers. Based on this principle, exfoliation methods can be categorized into three types: mechanical exfoliation, intercalation exfoliation, and etching exfoliation (Fig. 3).

3.1. Mechanical exfoliation for advanced anode materials in LIBs

Mechanical exfoliation involves the separation of layers in bulk materials by applying shear force, causing the breakdown of interlayer interactions (Fig. 3(a)) [47]. Graphene, one of the most popular 2D materials, was initially prepared through the mechanical exfoliation of highly oriented pyrolytic graphite using scotch tape [19]. Since then, numerous other materials have been successfully synthesized as 2D materials using this technique. For example, 2D phosphorene was obtained via mechanical exfoliation from black phosphorus [48], and single-layer molybdenum disulfide [49] was also prepared. Another method, ball milling, has been reported as a mechanical exfoliation approach. It has proven effective in producing graphene, MoS_2, WS_2, 2D nanosheets, and h-BN. Compared to scotch tape exfoliation, ball milling is more efficient and holds promise for industrial-scale production. However, a major drawback of ball milling is the relatively high contamination of the final 2D material due to the synthesis process.

3.2. Intercalation exfoliation for advanced anode materials in LIBs

Intercalation exfoliation is considered a viable technique for the mass production of ultrathin 2D materials (Fig. 3(a)). By introducing

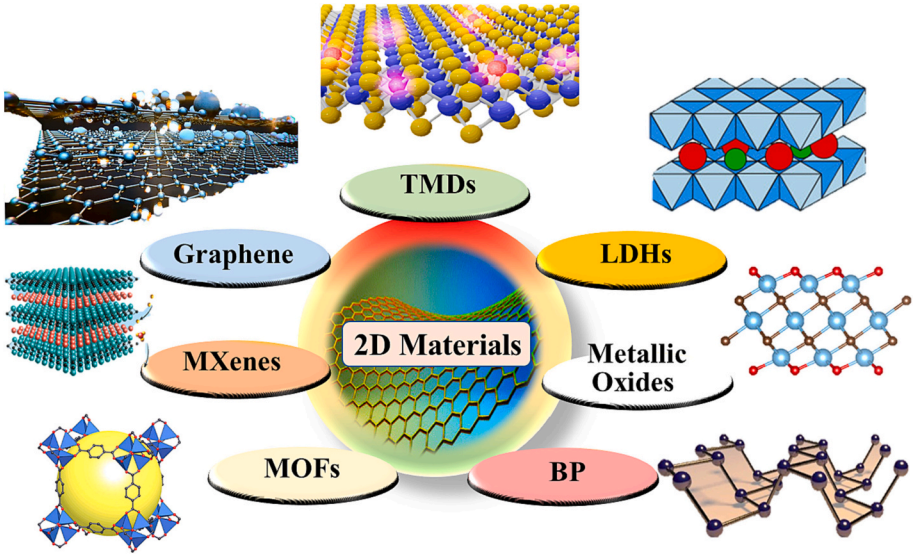

Fig. 1. Classification of 2D Nanomaterials for versatile energy applications.

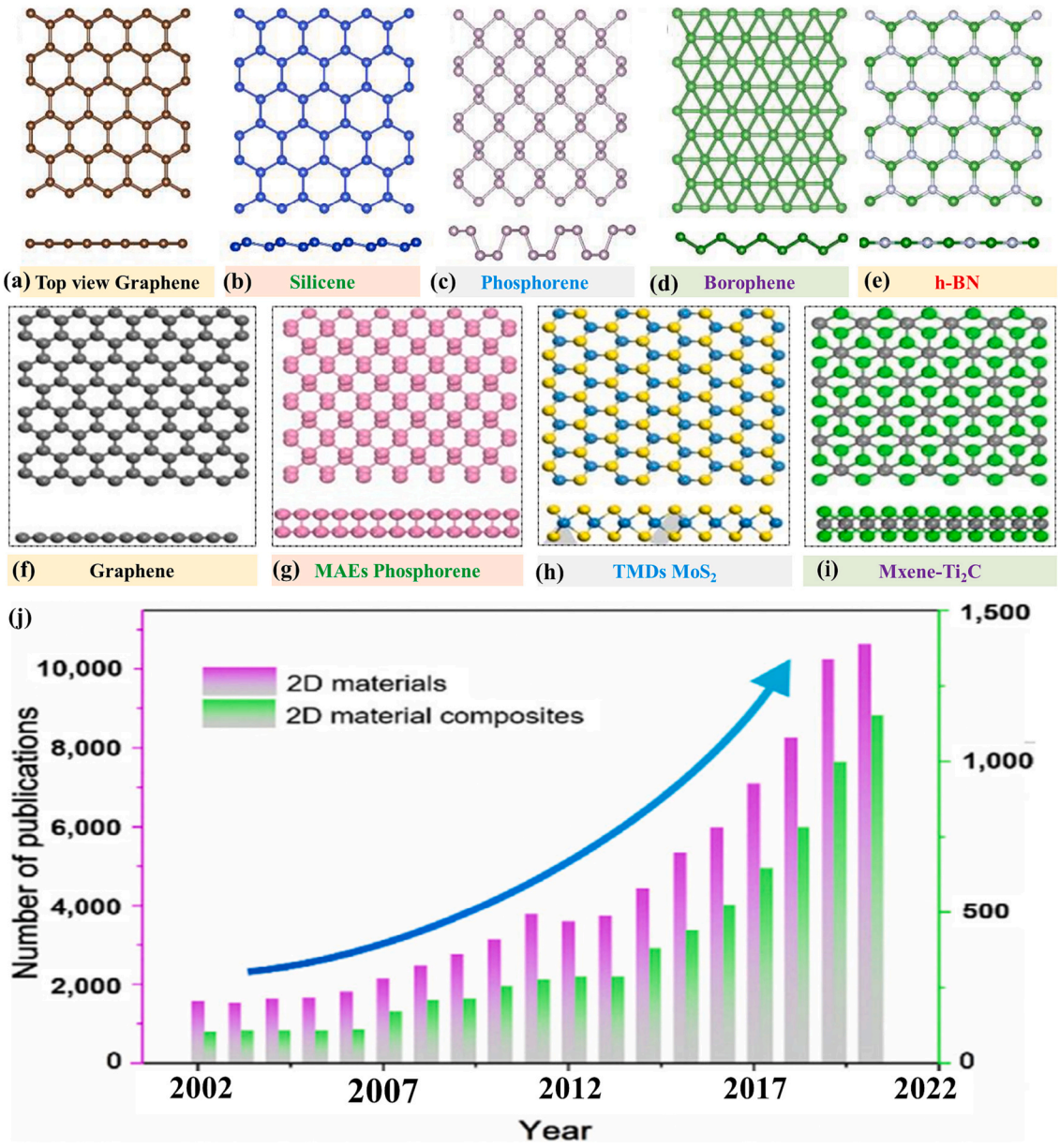

Fig. 2. Typical atomic structures, Top and side view of 2D mono layered (a). Top view graphene; (b). silicene; (c). phosphorene; (d). borophene; (e). h-BN; (f). Graphene; (g). MAEs; (h). TMDs; and (i). MXene-Ti_2C; Comparison of published papers chronologically for GO, MoS_2, WS_2, and phosphorene (j). [43].

additional ions and molecules into the precursor material, the interlayer forces are weakened, resulting in more efficient exfoliation. In the case of graphite, intercalation exfoliation involves the insertion of reductants and/or oxidants between the graphite layers to weaken their interaction and enable the production of graphene on a large scale through expansion and exfoliation. Similarly, mono-elemental analogues of graphene, such as arsenene, phosphorene, and antimonene, can be prepared from their 3D precursor materials due to the weak interlayer interaction [50]. For example, phosphorene synthesis was achieved by Chaban et al. using 1-ethyl-3-methylimidazolium tetrafluoroborate as a solvent [51]. This method can concurrently facilitate the detachment of phosphorene sheets and shield them from direct contact with environmental moisture and oxygen. This is attributed to the presence of amphipathic moieties and substantial shear viscosity. Intercalation methods can also be used for the synthesis of 2D transition metal dichalcogenides (TMDs). For instance, Coleman et al. demonstrated the intercalation of bulk TMD quartzes in commonly used solvents, resulting in the formation of single and few-layer nanosheets of dichalcogenides, such as WS_2, MoS_2, $MoTe_2$, $MoSe_2$, $TaSe_2$, $NiTe_2$, Bi_2T_3, and $NbSe_2$ [52]. Currently, liquid-phase exfoliation is frequently employed for the preparation of 2D composite materials. In particular, intercalation-assisted liquid-phase exfoliation represents an improved technique where pre-lithiated crystal precursors are utilized as predecessors.

3.3. *Etching exfoliation for advanced anode materials in LIBs*

Etching exfoliation, a top-down technique, is primarily used for the production of 2D MXenes (Fig. 3(a)). In general, MXenes are derived from MAX phases where the M-A bonds exhibit metallic properties. To prepare MXenes, a selective etching process is employed to break the M-A bond. The commonly used etchant for favorable leaching of the "A" layer from the MAX phase precursor is HF, which efficiently removes A-atom layers from MAX phases like Ti_3C_2. For example, Ti_3C_2 can be obtained from Ti_3AlC_2 by selectively etching out the Al layers using HF. However, alternative fluoride-free etchants have gained significant attention due to their environmentally friendly nature. Chloride ions

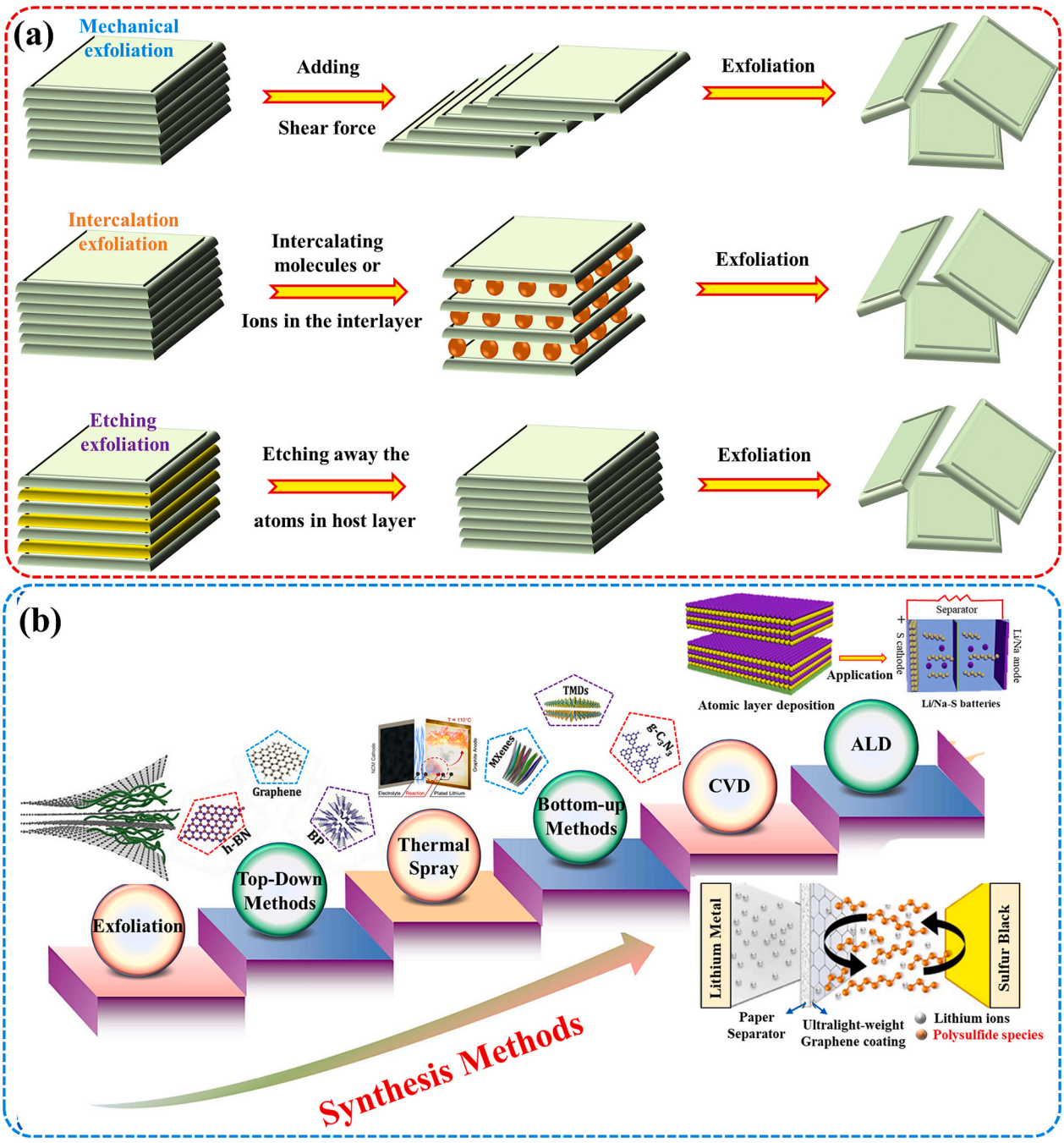

Fig. 3. Technique top-down methods schematic diagram for the preparation processes of 2D materials (a); synthesis techniques to prepare 2D materials (b).

have been successfully utilized to leach out Al and break the Ti—Al bond linkage. This delamination process has enabled the successful preparation of several MXene nanosheets, including V_2C, Nb_2C, and Ti_3CN. Additionally, in situ grafting-intercalating treatment has been employed to chemically functionalize Ti_3C_2 MXene with phenyl-sulfonic groups [53–56].

3.4. Bottom-up-approach in LIBs

The wet chemical hydrothermal/solvothermal technique is considered one of the most promising bottom-up approaches for fabricating 2D materials, including graphene, TMDs, and TMOs (Fig. 3(b)) [57]. Additional bottom-up techniques used for the fabrication of mono or bilayered nanosheets are chemical vapor deposition (CVD) and atomic layer deposition (ALD). In general, CVD provides better control over the thickness of the final product. An excellent example of this capability is the production of Mo_2C crystals, a type of MXene [100]. However, bottom-up techniques are not commonly employed for electrochemical energy storage applications due to their high cost, energy-intensive nature, and difficulties in scalability.

3.5. Comparative analysis of synthetic methods for practical applications of 2D Materials in LIB.

To provide an overview of various synthesis methods along with a comparison of their advantages and disadvantages, let's examine each method individually:

Chemical Vapor Deposition (CVD): Chemical vapor deposition

(CVD) involves depositing precursors in the vapor phase onto a substrate, where they react and form a solid film. CVD boasts several benefits, including the ability to produce high-quality, large-area 2D materials with precise control over thickness and properties. However, its complexity, requirement for high temperatures, specialized equipment, and longer production times are notable drawbacks.

Liquid Exfoliation: Liquid exfoliation involves mechanically or chemically breaking down layered bulk materials into 2D sheets dispersed in a solvent. This method is known for its versatility and capacity to create various 2D materials from bulk precursors. It offers a relatively straightforward and scalable approach to producing dispersed 2D materials. Nonetheless, challenges include achieving high-quality, large-area films and maintaining consistent thickness and quality due to the exfoliation process.

Sol-Gel Processes: Sol-gel processes encompass hydrolyzing and polymerizing precursor solutions to create a gel, which is then processed into thin films. This technique allows for controlled composition and thickness in thin films and finds applications in integrating 2D materials into composites. Disadvantages include difficulties in achieving uniformity and controlling the film's microstructure. The process can also be time-consuming and complex due to synthesis at elevated temperatures and pressures.

Hydrothermal and Solvothermal Methods: Materials are synthesized at elevated temperatures and pressures in a solvent using hydrothermal or solvothermal methods. These methods can yield crystalline and well-defined 2D materials with controlled properties, making them suitable for generating complex nanostructures. Drawbacks include challenges in controlling reaction conditions and potential limitations in scalability.

Mechanical Peeling (Scotch Tape Method: Mechanical peeling, often referred to as the Scotch tape method, involves manually removing layers from bulk materials using adhesive tape. While this technique can yield quality 2D materials with minimal defects, it is labor-intensive and not scalable for large-scale applications. It is better suited for basic research purposes.

Electrochemical Exfoliation: Electrochemical exfoliation involves applying an electric field to induce exfoliation of layered materials. This method is relatively fast and can produce exfoliated materials in situ for certain applications. However, its effectiveness depends on the electrical properties of the material and it can introduce defects in the resulting 2D sheets.

In choosing a synthesis method, factors to consider include desired properties, scalability, and practicality for lithium-ion battery (LIB) electrode materials. Generally, preferred methods are those that can generate high-quality, large-area films or dispersions with controlled thickness and composition. However, since different materials respond differently to various synthesis methods, the suitability of a method will also depend on the specific 2D material in use. To evaluate the performance of synthesized materials as LIB electrode materials, thorough characterization and electrochemical testing are essential.

4. The working principle of lithium-ion batteries

In general, lithium-ion batteries (LIBs) is a type of the prime rechargeable metal ion battery for energy storage applications. The process includes the conversion between chemical energy and electrical energy. LIBs were commercially introduced in early 1990s. Ever since, LIBs gained significant attention due to their unique properties including high working potential, large energy density, and long cycle life. Thus they are popular in plethora of applications and are nowadays considered irreplaceable in electronics (e.g., smartphones, laptops) and the future of mobility (e.g., battery powered vehicles). A typical LIB (lithium-ion battery) comprises various components, including electrodes (anode and cathode), a separator, different current collectors, an organic or inorganic electrolyte, and a battery case.

4.1. Exploring the dynamics: understanding the intricate charge-discharge mechanism of LIBs

In general, all batteries consist of two electrodes with different chemical potentials separated by an ionic conductive electrolyte. When an external load is applied to connect the two conductors, electrons naturally move from the anode to the cathode. To maintain charge balance, ions diffuse through the electrolyte, generating electrical energy through the external circuit. Lithium-ion batteries (LIBs) store electrical energy through the use of lithium intercalation (or insertion) compounds in both electrodes. This process is illustrated schematically in Fig. 4.

4.1.1. Anode charge storage mechanism

Understanding the power generation process entails delving into the role of the anode material. In this context, the anode material serves as a host for lithium ions. Let's delve into the discharge process for a more comprehensive understanding. During this phase, lithium ions traverse the electrolyte, moving from the anode to the cathode, while concurrently, electrons course through an external circuit in the reverse direction. These inherent processes find impetus in the electrochemical potential disparity between the positive and negative electrodes. The fundamental mechanism governing charge storage within the anode involves the intercalation of lithium ions into the framework of the anode material. A prevalent example of this phenomenon is observed in

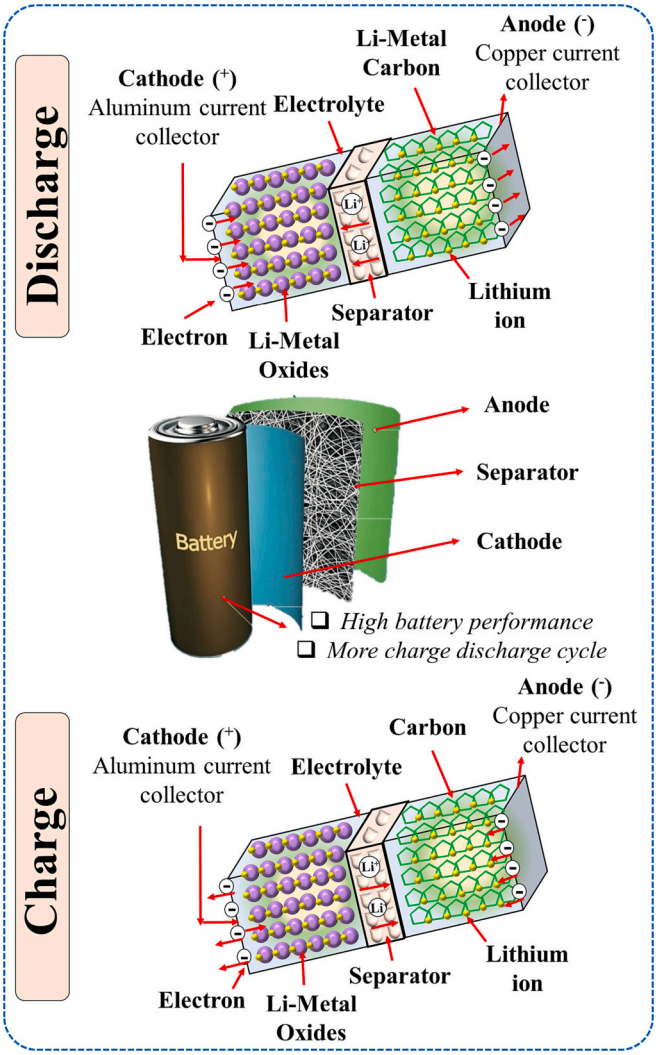

Fig. 4. Charge- discharge mechanism of li-ion battery [117].

the utilization of graphite as an anode material. In graphite, lithium ions intercalate amid the layers of carbon atoms, facilitating energy storage and subsequent release. This characteristic renders graphite a frequently employed material for anode applications.

4.1.2. Cathode charge storage mechanism

Upon charging, these processes undergo reversal propelled by an applied electric field or voltage. Within this context, the cathode material engages in a redox reaction, characterized by the transformation of transition metal dichalcogenide (TMD) ions (such as V, Zr, Mn) between varying oxidation states. This redox phenomenon, while upholding the structural cohesion of the cathode material, facilitates the reversible inclusion and removal of lithium ions. This pivotal interplay between the redox reaction and structural stability underpins the cathode's role in efficient energy storage. Lithium ions are extracted from the cathode and inserted into the anode, while electrons are conducted from the cathode to the anode through an external circuit, consuming electrical energy in the process. Enhancing the electrode materials can lead to improved electrochemical performance of lithium-ion batteries (LIBs), as the stable performance of LIBs heavily relies on the physical and chemical properties of advanced electrode materials. Researchers are exploring various electrically conductive materials to design LIB components such as anodes, cathodes, and electrolytes. LIBs outperform most other battery technologies in terms of energy density, often exceeding them by a factor of 2.5 [58]. Several factors contribute to the superior performance of LIBs. Firstly, the small ionic size of lithium (0.76 Å) enables easy insertion into the host matrix, facilitating efficient storage and release of lithium ions. Secondly, LIBs exhibit high energy and power densities, allowing for the storage of large amounts of energy and rapid release when required. Lastly, the low reduction potential of lithium (3.04 V versus a standard hydrogen electrode) contributes to the stability and reliability of LIBs [15].

An understanding of these charge storage mechanisms is crucial for the design of materials with high capacity, good cycling stability and fast charge and discharge rates. It will also help researchers to identify the challenges such as capacity fading, electrode degradation and safety concerns that are associated with certain materials and mechanisms.

5. Advancements in anode materials for lithium-ion batteries: composition-structure-property relationships

Two-dimensional materials are employed as anode materials in lithium-ion batteries to enhance the rate capacity and cycling performance of the batteries. Table 1 illustrates several examples of layered materials utilized as anodes in lithium-ion batteries.

The choice of specific two-dimensional (2D) materials, such as graphene, WS_2, MoS_2, and MXene, discussed in this review article can be influenced by various factors. Graphene, WS_2, MoS_2, and MXene are extensively researched 2D materials with significant potential across various applications, including lithium-ion batteries (LIBs). Their unique composition, structure, and electrochemical properties have garnered significant attention, rendering them pertinent candidates for an inclusive review. Inclusion in this review could stem from the availability of some 2D materials for experimental investigations and characterization. Factors such as cost-effectiveness and accessibility might contribute to their incorporation, while less affordable or less accessible materials might have received comparatively less attention. Furthermore, the selection of materials might have been influenced by their practical feasibility and potential for real-world LIB applications. Although certain transition metal oxides (TMOs) with lower costs could display promising properties, challenges related to their synthesis, stability, and performance might have restricted their consideration. The research trend toward graphene, WS_2, MoS_2, and MXenes was chosen due to their representation of prevailing directions in 2D materials research for energy storage. Their inclusion aids in directing ongoing research endeavors.

Comparative analysis: To provide readers with a holistic outlook on advancements across diverse material types, this review aims to conduct comparative analyses within specific categories of 2D materials, such as transition metal dichalcogenides, graphene-based materials, and MXenes. It's important to acknowledge that the selection of topics for review articles hinges on various factors, including research relevance, feasibility of experimentation, existing literature, and the article's particular objectives. While less costly transition metal oxides could be attractive options, their absence from this review might stem from factors like limited research focus, fewer established benefits, or unresolved challenges. Regarding the selection criteria, it's conceivable that they encompass a combination of material electrochemical performance, stability, theoretical capacity, available literature, and relevance to LIBs. For deeper insights into the specific rationale behind material selection, delving into the introduction and methodology sections of the article, where available, could provide valuable context.

To understand the potential of 2D materials for LIBs and to design new materials for future applications, it is essential to understand and discuss the composition-structure-property relationships. The study of these relationships can provide insight into how certain combinations of composition and structure lead to specific properties that are suitable for LIBs.

5.1. Composition-structure-property relationships in 2D materials for LIBs

Advancing the development of two-dimensional (2D) materials for lithium-ion batteries (LIBs) hinges on a comprehensive comprehension of the intricate interplay between composition, structure, and resultant properties. Composition governs the elements present and their relative proportions, which in turn wield significant influence over the material's electronic, thermal, and mechanical attributes. Correspondingly, the material's structure, encompassing facets like layer arrangement, defects, and crystal lattice orientations, holds paramount importance as it substantially shapes electrochemical performance, ion diffusion kinetics, and cycling stability. The collective impact of composition and structure resonates in the resultant properties, encompassing factors like specific capacity, rate capability, and cyclability.

In the realm of LIB electrode materials, there isn't a singular combination of composition and structure that stands as universally ideal. Nonetheless, overarching trends do exist, offering guidance for material design. For instance, materials featuring a layered structure that facilitates ion intercalation and diffusion often garner preference. Furthermore, a delicate equilibrium between elevated specific capacity and structural stability proves pivotal in averting capacity deterioration during cycling. Considering safety, the selection of composition and structure acquires added significance, particularly in light of materials prone to unstable intercalation or side reactions, which can potentially

Table. 1
2D material recorded as anode in Li-ion batteries.

No	Type of 2D	2D Materials and composites	Ref
1	Graphene and its analogous	Graphene (G) Fluorinated reduced graphene (FG) Reduced-graphene oxides (RGO), Graphene oxide (GO) Hexagonal boron-nitride nanosheet (BNNS), Hexagonal boron carbon nitride nanosheet (BCN)	[59]
2	Metal oxides/ hydrides	MoO_3, SnO_2, VO_2, WO_3, NiO, Ni $(OH)_2$, MnO_2, V_2O_5, TiO_2, Co_3O_4, Bi_2O_3.	[60,61]
3	Chalcogenides	GaSe, GaS, MoN, CoSe, MoS_2, NiS, NiSe, SnSe, WSe_2, WS_2, TiS_2, SnS_2, VS_2, GeSe, $MoSe_2$, $NbSe_2$, Bi_2Se_3, $MoTe_2$.	[62,63]
4	MXene	Ti_2C, Ti_3C_2, Nb_2C, TaC_2, V_2C, Ti_3CN, Ti_2N.	[64,65]
5	Mono elements	P, Si, Ge, B, Sb hexagonal boron nitride (h-BN)	[66]

pose hazards.

To forge a path toward novel 2D materials tailored for forthcoming LIBs, an inclusive strategy is recommended. Computational modeling can predict the electrochemical behavior of assorted compositions and structures, aiding in the identification of auspicious candidates for synthesis. Subsequent to this predictive phase, iterative experimental validation emerges as an imperative step. It serves to corroborate forecasted properties, while also uncovering potential deviations. The amalgamation of theoretical insights with empirical substantiation forms a powerful guide, steering the development of bespoke materials optimized in terms of composition, structure, and properties for LIB applications. In the grander scheme, this approach substantially contributes to the ongoing evolution of battery technology.

5.2. Strategies for enhancing electrochemical performance through structure-activity relationship:

Certainly, Progressing the electrochemical performance of materials within lithium-ion batteries (LIBs) necessitates a profound grasp of the intricate interplay between material structure and activity. Unveiling the structure-activity relationship stands pivotal in tailoring materials with augmented capacity, cyclability, rate capability, and overall longevity. Several strategies harnessing this relationship are delineated below:

Optimized Morphology and Composition: The electrochemical behavior of electrode materials is profoundly influenced by their morphology and composition. Prudent manipulation of particle size, morphology, and composition can amplify ion diffusion kinetics, accommodate volume fluctuations during cycling, and alleviate mechanical stresses, culminating in enhanced cycling stability and capacity.

Surface Engineering: Surface modifications and coatings wield influence over the material's interaction with the electrolyte and side reactions. The incorporation of atomically thin protective layers or conductive coatings can ameliorate stability, electronic conductivity, and overall electrochemical performance.

Defect Engineering: Controlled introduction of defects or vacancies can modulate ion diffusion paths and charge transport properties. This endeavor can enhance ion accessibility and bolster the capacity retained over cycling.

Layered Structures: Layered materials, encompassing the likes of 2D entities like MXenes and transition metal dichalcogenides (TMDs), present unique intercalation domains for lithium ions. The manipulation of interlayer spacing and crystal structure can optimize ion diffusion pathways and augment capacity.

Porous Architectures: Porous structures, encompassing mesoporous or nanoporous materials, offer elevated surface areas and expedite ion transport. The tailoring of porosity heightens electrolyte accessibility, thereby facilitating swifter charge and discharge rates.

Alloying Reactions: Materials engineered for alloying reactions, exemplified by silicon-based anodes, hold the promise of escalated capacity. However, meticulous management of volume changes during lithiation and delithiation proves instrumental in upholding structural integrity.

Ion-Redox Mechanisms: Cathode materials operating via ion-redox mechanisms, exemplified by transition metal oxides, can deliver elevated capacity. The manipulation of crystal structure and the regulation of oxygen activities can amplify the reversibility of redox reactions.

Embarking on these strategies within the framework of the structure-activity relationship empowers researchers to make judicious decisions while crafting novel materials or optimizing existing ones. The synergy of computational modeling and advanced characterization techniques occupies a pivotal role in deciphering the intricate ties between material structure and electrochemical performance. By methodically unraveling these relationships, researchers can expedite the advancement of high-performance electrode materials, thereby propelling the evolution of LIB technology.

5.3. Advancements in graphene-based anode material for LIBs

Natural and synthetically prepared graphite are used as electrode materials for batteries with a suitable specific capacity of 372 m Ahg ^{1} [67]. Su et al. [68] produced a single layer of graphite, known as graphene, for the first time using the mechanical exfoliation method. The finding in this direction has escorted in a “graphene frontier”, with a universal concentration in exploiting its inimitable electronic properties for probable applications in energy storage and microelectronics. As graphene possesses excellent mechanical flexibility and electrical conductivity, it finds applications as an electrode and as a modifier for electrode materials, leading to the development of highly conductive composite materials with improved electrochemical properties. According to a study by Yoo et al., graphene flakes have demonstrated effective mitigation of volume expansion in metal and metal oxide anode materials during the charge and discharge process, resulting in improved electronic conductivity [69]. This study further revealed the electrochemical lithium intercalation behavior in graphene nanosheets. Additionally, Lian et al. [70] and Yoo et al. [69] have explained how the introduction of nanotubes and fullerenes between graphene layers increases the layer-to-layer distance, which is favorable for achieving high reversible capacities of 800 m Ahg ^{1}. More recently, there has been a focus on the conductive modification of $LiFePO_4$, driving further research in this area.

In a study conducted by Wang et al. [71], graphene/$LiFePO_4$ nanocomposites were synthesized using the solvothermal and hydrothermal methods. The researchers achieved a specific discharge capacity of 160.3 mA h g ^{1} at a current density of 0.1C and 81.5 mA h g ^{1} at 10.0C. Raman spectroscopic analysis demonstrated that the 8 % graphene composite exhibited a high distribution of sp^2 hybrid carbon atoms. The porous structure between graphene nanosheets and $LiFePO_4$ particles allowed for effective electrolyte penetration, which positively influenced the electrochemical performance. The presence of numerous gaps between the graphene nanosheets and $LiFePO_4$ particles facilitated the movement of Li + ions, thus enhancing the battery's electrochemical performance.

In a corresponding study, Sue et al. [72] fabricated $LiFePO_4$/graphene and $LiFePO_4$/Carbon composites as anodes and observed that the electrochemical performance of the 2 % graphene composite surpassed that of the 20 % graphene composite. This result can be attributed to the “point-to-point” mode of conduction formed by the former material, which establishes a more efficient conductive network. On the other hand, the latter material exhibits a “point-to-point” mode of conduction. Graphene demonstrates great potential as an encapsulating material for Li storage due to its excellent conductivity, large surface area, high flexibility, and notable chemical stability.

Wang et al. [73] presented an economical and straightforward approach for producing germanium@graphene@TiO_2 core-shell nanofibers (Ge@G@TiO_2 NF) as negative electrode materials for lithium-ion batteries (LIB) and sodium-ion batteries (SIB). The Ge@G@TiO_2 composites exhibited significantly enhanced electrochemical performance in both LIB and SIB systems. The fabrication process involved electrospinning followed by atomic layer deposition (ALD) (Fig. 5(a)). This unique design offers several advantages. Firstly, the use of graphene-doped nanofibers as an electrolyte blocking layer serves two purposes: preventing the formation of a solid electrolyte interphase (SEI), resulting in a high coulombic efficiency (CE) of 99.84 %, and providing mechanical support and a conductive pathway. Secondly, the outer shell of TiO_2 encapsulates the Ge@G core, ensuring structural integrity. Lastly, the combination of graphene and TiO_2 provides dual protection for the germanium nanofibers, effectively mitigating the volume expansion issue during the charge and discharge processes. The Ge@G@TiO_2 composite demonstrates a remarkable enhancement in electrochemical

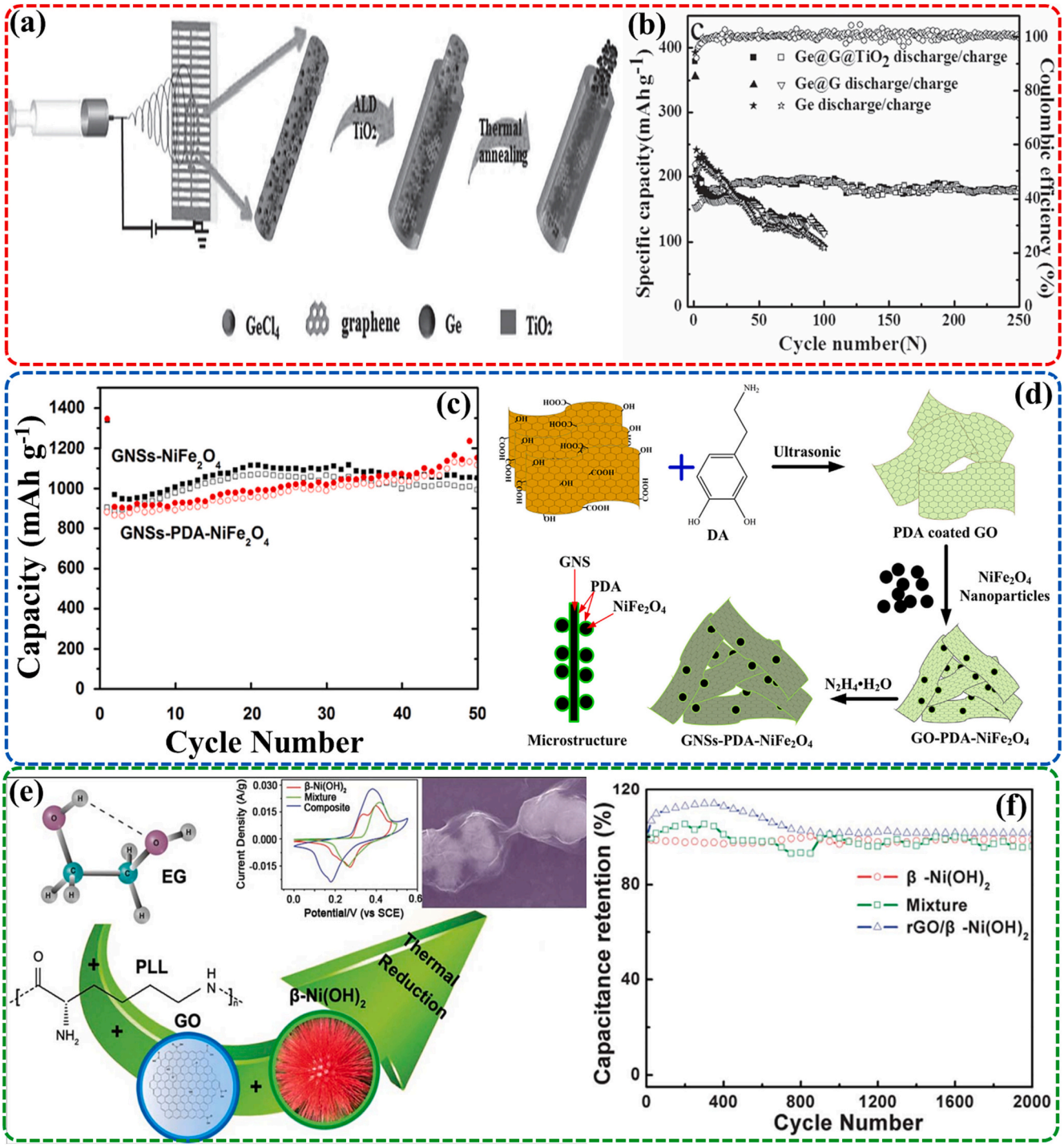

Fig. 5. Schematic diagram of the fabrication process of Ge@G@TiO_2 NFs (a); The cycling performance of different materials at a current density of 100 mA g^{-1} (b) [73]; The stability of GNSs–$NiFe_2O_4$, GNSs–PDA–$NiFe_2O_4$, and $NiFe_2O_4$ (c); The possible formation mechanism of GNSs–PDA–$NiFe_2O_4$ nanocomposite (d) [75]; The formation process of the rGO@bNi$(OH)_2$ composite (e); the cycling performance of composite electrodes rGO@β-Ni$(OH)_2$, β-Ni$(OH)_2$ and the mixture, rGO@b-Ni $(OH)_2$ is measured @ 5.33 Ag^{-1} (f) [76].

performance for both LIBs and SIBs. Table 2 illustrates the list of graphene being used as an anode in Li-ion applications.

The Ge@G@TiO_2NFs demonstrate an initial discharge capacity of 1701 mA h g ^{1}, which is well maintained at 1050 mA h g ^{1} in LIB after 100 cycles. Similarly, in SIB, the capacity remains at 368 mA h g ^{1} after the first discharge, exhibiting decay rates of only 0.13 % and 0.04 % with each cycle. After 250 cycles, the capacity reaches 182 mA h g ^{1} (Fig. 5(b)). The incorporation of protective graphene and TiO_2 layers on Ge or Ge@G significantly enhances the cycling stability, with the Ge@G@TiO_2 composite demonstrating the best performance by retaining a capacity of 1050 mA h g ^{1} after 100 cycles. These results clearly indicate the significant improvement in cycling properties achieved through the incorporation of graphene and TiO_2 layers.

Furthermore, Xiao et al. [75] developed graphene/$NiFe_2O_4$ (GNSs-PDA-$NiFe_2O_4$) nanocomposites functionalized with polydopamine (PDA) using an in-situ ultrasound method (Fig. 5(d)). The subsequent GNSs-PDA-NiFe2O4 nanocomposites exhibited reversible capacities of up to 947 mA h g ^{1} with significantly improved rate performance.

Table 2
Some recorded graphene as anode for Li-ion applications.

No	Anode material	Synthesis method	Capacity (mA h g ^{1})/ energy density (A g ^{1})	Ref
1	Pure graphene	–	200–600 @ 0.1C	[9]
2	Multilayer graphene spheres	Scalable graphitization strategy	401.4 mA h g ^{1} @ 0.1 A g ^{1}	[10]
3	Oxidized GNRs	Unzipping technique, solution-based oxidative process	1400 @ 0.05C and 600 mA h g ^{1} after 10 cycles	[74]
4	Nonmetal@graphene		900–2000 @ 0.1C	[12]
5	GNS + CNT	Heat treatment at 800 °C for 2 h	730 @ 0.05C and 480 mA h g ^{1} after 20 cycles	[73]
6	CNT@graphene		300–700 @ 0.1C	[75]
7	Si@G	Chemically anchoring	2158 mA h g ^{1}, 1168 mA h g ^{1} after 30 cycles	[76]
8	Si@G@carbon	Freeze-dried, thermal annealing	2246 @ 0.1C and 1000 after 70 cycles	[77]
9	Si@crumpled graphene	One-step capillary-driven assembly route	940 @ 1C after 250 cycles	[78]
10	Si–rGO stratum structure	Liquid exfoliated	1500 @ 1.35C after 100 cycles	[79]
11	Siliconnanowire@graphene sheath@reduced graphene overcoat	Encapsulation of silicon nanowires (SiNWs) with dual adaptable apparels	1650 @ 0.84C after 50 cycles	[80]
12	G@Si@CNFs	In situ reduction followed by a dealloying process.	1792 @ 0.1C, 897 mA h g ^{1} after 200 cycles	[81]
13	Si/reduced graphene oxide		780 @ 7.2C after 300 cycles	[82]
14	Multilayered Si@RGO	Dip-coating method	2300 mA h g ^{1} @ 0.05C	[83]
15	Si@template carbon-bridged oriented graphene		1390 @ 2C after 200 cycles	[84]
17	SnO_2@N-doped rGO	In situ hydrazine monohydrate vapor reduction method	1865 @ 0.5C, 1074 mA h g ^{1} after 500 cycles	[85]
18	Sn@N-doped reduced graphene oxide	Facile method	481 @ 0.1C after 100 cycles	[86]
19	Co_3Sn_2@Co–N-doped graphene	Hydrothermal synthesis	1651 @ 0.25 after 100 cycles	[87]
21	Sn@porous graphene networks	In situ chemical vapor deposition (CVD)	682 @ 2C after 1000 cycles	[88]
22	FeS@reduced graphene oxide	Facile direct-precipitation approach	978 @ 0.1C after 40 cycles	[89]
23	Cobalt sulfides@graphene nanosheet	Facile sol–gel route	950 @ 0.1C after 100 cycles	[90]
25	Co_3O_4@G	Hydrothermal technique electrostatic self-assembly process.	1304 mA h g ^{1} @ 0.2 A g ^{1}, 1113 mA h g ^{1} after 100 cycles	[91]
27	Fe_2O_3@rGO composite	Homogeneous precipitation	1693 mA h g ^{1} @ 0.1 A/g, 1027 mA h g ^{1} after 50 cycles	[92]
29	TiO_2 nanotube@N-doped graphene	One-step and scalable method hydrothermally	369 @ 0.1C after 180 cycles	[93]
31	MoS_2@graphene composite	l-cysteine-assisted solution-phase method	1571 mA h g ^{1} @ 0.1 A g ^{1}, 1187 mA h g ^{1} after 100 cycles	[94]
32	Sb_2O_3@rGO	Alcohol dissolution-reprecipitation method	2260 mA h g ^{1} @ 0.1 A g ^{1} 808 mA h g ^{1} after 120 cycles	[95]

Specifically, a capacity of 562 mAh g ^{1} was achieved at 5 A h g ^{1}, which is about 7 times higher than the capacity of graphene/$NiFe_2O_4$ nanocomposites (Fig. 5(c)). This improvement is attributed to the strong interactions, conducting network, and enhanced wettability with electrolytes achieved by functionalizing the graphene with polydopamine. The incorporation of GNSs-PDA-$NiFe_2O_4$ as an anode material offers a new approach to enhancing the charging performance of Li-ion batteries.

Li et al. [76] employed a solvothermal method to synthesize highly efficient hybrid composites of rGO@$Ni(OH)_2$.(rGO@$Ni(OH)_2$). The synthesis process involved the deposition of hollow β-$Ni(OH)_2$ microspheres onto rGO foils, utilizing poly(L-lysine) (PLL) as a reducing agent and ethylene glycol (EG) as a coupling agent (Fig. 5(e)). The resulting β-$Ni(OH)_2$@reduced graphene oxide composite exhibited promising lithium storage properties, demonstrating a capacity of 927 mAh g ^{1} (Fig. 5(f)). However, the composite exhibited relatively poor capacity retention, with only 54.7 % retention after 30 cycles.

6. Advancement in WS_2 as anode materials for LIBs

As mentioned previously, layered transition metal monochalcogenides (LTMs), which are single-element analogues of graphene, exhibit strong intralayer covalent bonds and weak van der Waals forces between the layers. This unique structure provides ample space for the insertion of Li-ions. Similarly, 2D transition metal dichalcogenides (TMDs), specifically MX_2 (M = W, Mo, Ti, V, Fe, Ni, Mn, Zn; X = Se, S) such as MoS_2 and WS_2, consist of three atomic layers stacked together. Metallic layers are sandwiched between two layers of sulfide "X" in the crystal structure (S–Mo–S, S-W-S). These layers are held together by van der Waals forces, enabling them to exhibit fast-ion conductivities and facilitating the lithiation/de-lithiation of Li^+ ions. Due to these remarkable properties, TMDs have garnered significant attention in recent years for their research and practical applications.

TMDs have gained considerable attention in the field of energy

storage due to their ability to undergo 4-electron transfer reactions in electrochemical methods [96]. The stacked S-W-S sheets in TMDs, such as MoS_2 and WS_2, exhibit larger interlayer distances (002) (d = 0.62 nm) compared to commonly used graphite (0.34 nm). This expanded spacing greatly facilitates the diffusion of Li-ions, making TMDs highly suitable for electrochemical applications. While MoS_2 has been extensively studied in this context, WS_2 is a relatively newer material that holds promise. WS_2's underlying nanosheet crystal structure also possesses intriguing electronic and optical properties, including strong spin-orbit interactions, tunable bandgaps, and high carrier mobility [97]. Unlike graphene, bulk crystals of tungsten disulfide (WS_2) are semiconductors with an indirect energy bandgap. However, single-layer WS_2 exhibits a direct bandgap of 1.1 eV, which aligns well with previous research findings.

TMDs, particularly transition metal disulfides (MS_2, where M = W, Mo, Mn, Fe, Zn, Ni, etc.), exhibit higher electrical conductivity compared to metal oxide counterparts. Additionally, they have a high theoretical specific capacity of approximately 433 mA h g^{-1} based on the insertion of 4 mol of Li ions, surpassing commercial graphite (372 mA h g^{-1}) and other carbon/graphite-based materials. These properties make TMDs, such as WS_2, promising alternatives to graphite as negative electrode materials for reversible energy storage, especially in lithium batteries (LBs) [98]. In contrast to well-studied MoS_2, WS_2 demonstrates substantial intrinsic electrical conductivity without significant volumetric expansion during Li-ion intercalation. This characteristic contributes to improved structural stability during repetitive lithiation/delithiation processes [5]. WS_2 has been effectively employed as an anode material in various alkaline ion-battery systems, including lithium-ion batteries, potassium-ion batteries, and sodium-ion batteries, owing to its rapid Li^+ diffusion and storage capability. The 2D structure of WS_2 offers multiple active sites, which enhances the electrochemical performance in lithium-ion batteries. However, its poor rate performance and fast capacity decline currently limit its widespread use in practical applications for LIBs [99].

Various approaches have been proposed to address these challenges. One approach involves the conversion reaction process, where lithium ions and electrons are gathered in the form of lithium sulfide and metallic tungsten [99]. The utilization of WS_2-based complex composites as negative electrode materials has proven to be effective [98–101]. Strategies such as connecting WS_2 with non-active or less active secondary materials can significantly accommodate the strains and stresses that arise from lithium intercalation in WS_2, while also improving the electrochemical reaction kinetics. For instance, Feng et al. [101] fabricated tungsten disulfide nanoflakes as negative electrode materials for LIBs, achieving a high reversible capacity of 680 mA h g^{-1} over 20 cycles. Srinivaas et al. synthesized highly rich few-layered nanoflowers (NFs) of 1 T WS_2 phase, demonstrating a very high initial capacity of approximately 890 mA h g^{-1} with stable cyclic performance as anode materials for LIBs [102]. In another study, Kim et al. [103] prepared a WS_2-nanoflowers/rGO composite, where mono and a few layers of WS_2 were integrated into carbon fibers through a facile electrospinning technique. The composite exhibited outstanding capacity retention, maintaining a capacity of 437.5 mA h g^{-1} after 200 cycles at a current density of 0.5 A g^{-1}.

In 2012, a novel organic polymer composite called graphitic carbon nitride (g@C_3N_4), which exhibits a graphene-like structure, was developed as an anode material. This material has gained significant interest due to its composition rich in metal-free elements (N and C), its conjugated assembly, and its high chemical stability [101–103]. In addition to its role as a good anode material, W_2C also acts as an efficient catalyst. When grown on CNTs, it demonstrates excellent photo-electrocatalytic performance for the hydrogen evolution reaction (HER). Material simulation results have shown that W_2C exhibits ultra-fast lithium ion diffusion with low diffusion resistance of approximately 0.045–0.13 eV. Therefore, the combination of W_2C and WS_2 is expected to yield a promising anode material for lithium-ion batteries (LIBs).

Furthermore, WS_2 possesses another advantageous characteristic, which is its lower volume expansion compared to other metal complexes, making it suitable for LIBs. To enhance electronic conductivity and minimize the volume expansion, we employed a coating approach of WS_2 using polymer-derived carbon, which improved the structural stability of the material [99]. To evaluate the electrochemical performance, a half coin cell was fabricated using WS_2@PEI as the negative electrode for a lithium-ion battery. However, this setup generated a significant amount of heat, leading to elevated battery temperatures. The excessive heat could cause short-circuiting, high temperatures, and poor specific capacity, severely damaging the system [104,105]. Therefore, it is crucial for the polymer skeleton to possess thermal stability to mitigate the risks of polymer melting at high temperatures [252].

Among various engineering plastics, the amorphous polymer polyetherimide (PEI) stands out due to its excellent mechanical properties, stable thermoxidative characteristics, and high thermal stability. Additionally, there is a favorable affinity between WS_2 nano-sheets and PEI due to the presence of amide and ether bonding in the molecular chains of PEI. Therefore, selecting PEI as the composite skeleton can provide WS_2@PEI with enhanced thermal stability for high-performance lithium-ion batteries [104]. Table 3 presents examples of WS_2 used as an anode in Li-ion batteries.

7. Advancement in MoS_2 as anode material for LIBs

TMDs such as MoS_2, possess a layered structure where metal atoms are sandwiched between sulfide layers (S-Mo-S), held together by weak van der Waals forces. MoS_2 can be considered as a graphene monolith with embedded MoS_2 layers [128]. This material exhibits a unique three-layer atomic structure and offers advanced intrinsic fast ionic conductivity compared to metal oxides. Additionally, MoS_2 demonstrates a higher theoretical capacity of 670 mA h g^{-1} compared to graphite. These characteristics make it a promising candidate for various applications, including energy storage, based on the following equations.

Charge (lithium) storage mechanism

$$MoS_2 + 4Li^+ + 4e^- \leftrightarrow Mo + 2Li_2S \quad (1)$$

$$MoS_2 + xLi^+ + xe^- \leftrightarrow Li_xMoS_2\ (\sim 1.1\ \mathrm{V@Li}/Li^+) \quad (2)$$

$$Li_xMoS_2 + (4 \quad x)Li^+ + (4 \quad x)e^- \leftrightarrow Mo + 2Li_2S \quad (3)$$

The charge storage phenomena in MoS_2 can be revealed through in situ XRD and XAS techniques. The morphology of MoS_2 nanosheets bears some resemblance to that of graphene. These nanosheets show great potential for electrode applications in batteries. The electronic properties of TMDs, including MoS_2, can vary depending on the filling of d-band electrons, leading to metallic, semiconducting, superconducting, or insulating behavior. However, pristine MoS_2 typically exhibits low electrical conductivity, which hampers rapid electron transfer and makes it unsuitable for efficient energy storage in lithium batteries. Additionally, bulk MoS_2 suffers from sluggish kinetics and large volume changes during charge/discharge cycles, resulting in poor cyclic stability. MoS_2 crystals can be reduced to single or few-layer structures at the nanoscale. This reduction in thickness from bulk to monolayer-single layers induces a transition from an indirect bandgap to a direct bandgap, known as the quantum confinement effect. As a result, the bandgap circumference of MoS_2 increases. Two-dimensional MoS_2 nanosheets with a high surface-to-volume ratio facilitate tight electrode-electrolyte connections and short diffusion paths for Li^+ ions. Structural studies have identified three different phases of MoS_2: 1 T-, 2H-, and 3R-MoS_2. The 2H- and 3R-MoS_2 phases exhibit a trigonal prismatic arrangement of molybdenum atoms. The highly stable 2H-MoS_2 phase possesses distinct optical properties, such as photoluminescence peaks at an energy of ~1.9 eV, consistent with its bandgap. However, bulk MoS_2

Table. 3
Some recorded WS_2 as Anode for Li-ion batteries.

No	Anode material	Synthesis method	Specific capacity (mA h g^{-1}) and cyclic stability (A g^{-1})	Ref
1	Commercial WS_2	–	300 mA h g^{-1} @ 0.1C after 60 cycles	[106]
2	Few layered WS_2	(Jet cavitation of commercial WS_2)	489 mA h g^{-1} @ 0.1 after 60 cycles	[107]
3	WS_2@HNCSs	Facile gas-solid reaction	801.4 mA h g^{-1} @ 0.1	[108]
4	WS_2-RGO	Hydrothermal synthesis	400–450 mA h g^{-1} @ 0.1 after 50 cycles	[109]
5	WS_2@RGO	Hybrid microwave annealing	512 mA h g^{-1} @ 5	[110]
6	Sulfurized WS_2	Low-temperature and scalable sulfuration method	566.8 mA h g^{-1} @ 0.8 after 50 cycles	[111]
7	Hexagonal WS_2 nanosheets (650 °C)	Colloidal precipitation	216 mA h g^{-1} @ 1C after 20 cycles	[112]
8	WS_2	Hydrothermal method.	381.7 mA h g^{-1} @ 0.8 after 50 cycles.	[113]
9	2D WS_2 nanosheets	(Calcination of W and S powder)	194 mA h g^{-1} @ 2.5C after 1000 cycles	[114]
10	PDPC/WS_2	Chemical vapor synthesized	478 mA h g^{-1} @ 0.1 after 70 cycles	[115]
11	WS_2-nanoflowers@rGO	Freeze-drying assisted method.	730 mA h g^{-1} @ 0.1 after 150 cycles	[116]
12	WS_2-graphene nanosheets	Colloidal synthesis	596 mA h g^{-1} @ 1C	[117]
13	WS_2@C@RGO	Colloidal synthesis	402 mA h g^{-1} @ 1C	[118]
14	WS_2-nitrogenated graphene	Sol-gel method	750 mA h g^{-1} @ 1C	[119]
15	WS_2@g-C_3N_4	Solid-state reaction method	1229.8 mA h g^{-1} @ 0.1, 622.7 mA h g^{-1} after 400 cycles	[120]
16	WS_2 nanoflakes	Rheological phase reaction	680 mA h g^{-1} and 0.045 mA h g^{-1} after 20 cycles	[121]
17	Double-layer WS_2@hollow carbon	In situ hydrothermal method	987 mA h g^{-1} @ 0.1	[122]
18	Mesoporous WS_2@carbon nanofibers	Electrospinning and sulfurization	754 mA h g^{-1} @ 0.5 after 120 cycles	[123]
19	W_2C@WS_2 alloy nanoflowers (NFs)	Facile hydrothermal method	1040 mA h g^{-1} @ 0.1	[124]
20	PCS@WS_2@NG	Hydrothermal method.	205.0 mA h g^{-1} @ 0.5 after 900 cycles	[125]
21	(WS_2@C)	Ball-milling and sulfidation.	322 mA h g^{-1} @ 0.2 after 100 cycles	[126]
22	WS_2@NC	Via sol gel method	712 mA h g^{-1} @ 0.1	[127]
23	WS_2@(N-doped) graphite	Gas-phase sulfurization	963 mA h g^{-1} @ 0.043	[127]
24	Mesoporous WS_2	Vacuum assisted impregnation route	805 mA h g^{-1} @ 0.1C	[123]
25	WS_2 CMK-3 matric	Wet chemical method	720 mA h g^{-1} @ 0.1 after 100 cycles	[12]

in the 2H phase exhibits low electrical conductivity.

The electrochemical performance of MoS_2 in its 2H phase presents several challenges that need to be addressed. Firstly, the inherent low electronic conductivity of the highly stable 2H phase of MoS_2 negatively impacts battery performance, resulting in limited rate capability and hindered charge transfer processes. Secondly, the degradation of MoS_2 during charge/discharge cycles further deteriorates its electrochemical performance. These challenges highlight the need for strategies to improve the conductivity and stability of MoS_2 for enhanced battery performance. Lastly, the tendency of 2D MoS_2 to aggregate reduces the available surface area and hampers ion transport. Additionally, the low mechanical strength of MoS_2 nanosheets makes them prone to excessive stress, resulting in restacking and structural degradation, leading to rapid capacity fading [129].

However, the distinctive morphology and structure of 2D MoS_2 also offer several advantages. Firstly, the considerable specific surface area of MoS_2 nanosheets provides a multitude of active sites for electrochemical reactions. Secondly, the substantial interlayer spacing of ~0.62 nm enables fast intercalation and extraction of metal ions, while also accommodating the volume expansion that occurs during the intercalation process. Lastly, the ultra-thin thickness and flexibility of MoS_2 make it suitable for flexible energy storage applications [130]. Numerous approaches have been explored to enhance the electrochemical performance of MoS_2, with most research focusing on the following strategies:

Hierarchical nanostructures: Preparation of hierarchical nanostructures helps prevent restacking of MoS_2 nanosheets and increases the specific surface area, providing more active sites for electrochemical reactions.

Hybridization with conductive materials: Combining MoS_2 with highly conductive materials like carbon or graphene-based nanomaterials promotes electron transfer and maintains the structural integrity of the composite, leading to improved electrochemical performance.

Composite formation: Forming composites of MoS_2 with other electroactive materials creates synergistic effects that enhance cyclic stability and overall capacity of the electrode material.

Interlayer spacing optimization: Increasing the interlayer distance in MoS_2 allows for the accommodation of more ions and electrons, facilitating faster ion transport rates during charge and discharge processes.

Metallic phase formation: Creating a metallic phase of MoS_2 can significantly improve its conductivity, and electrochemical rates, and ultimately increase the capacity of the material.

However, it should be noted that the limited theoretical capacity of graphite remains a challenge for achieving high-energy lithium-ion batteries (LIBs).

Qu et al. conducted a synthesis of MoS_2 nanosheets decorated with ultrasmall Fe_3O_4 nanoparticles using a two-step hydrothermal method [131]. The resulting composite, MoS_2/Fe_3O_4, demonstrated the ability to accommodate volume variations during cycling, facilitating electrolyte penetration and faster lithium-ion transport. The incorporation of Fe_3O_4 nanoparticles acted as barriers, preventing restacking of MoS_2 nanosheets and minimizing the agglomeration of MoS_2 nanowires. This arrangement allowed the anode material to accommodate volume expansion during charging and discharging, resulting in a large capacity.

Hybrid anodes composed of Fe_3O_4/MoS_2 exhibited high reversible capacities of 224 and 1033 mA h g^{-1} at current densities of 2 and 10 A g^{-1}, respectively. Various methods such as atomic layer deposition (ALD), chemical vapor deposition (CVD), thermal pyrolysis, and hydro/solvothermal techniques have been employed to fabricate MoS_2-based nanohybrids for battery applications. Additionally, it is worth noting that the volume changes of MoS_2 during lithiation were found to be approximately 103 %, which is significantly lower than that of metal alloying materials such as silicon (420 %).

Nanostructure engineering and carbon modification have been

investigated as strategies to overcome the challenges related to the rapid capacity decay and structural degradation of MoS_2 during electrochemical reactions. One approach to mitigate the agglomeration of MoS_2 is to incorporate carbon-based materials into the system along with transition metal dichalcogenides (TMDs). This incorporation of carbon-based materials with TMDs offers potential solutions to improve the stability and performance of MoS_2-based electrode materials.

Carbon-based composites with MoS_2 are categorized into four types based on the dimensionality of carbon, namely MoS_2@0D carbon, MoS_2@1D carbon, MoS_2@2D carbon, and MoS_2@3D carbon. These composites have exhibited promising electrochemical properties. To enhance the performance, Lou et al. employed a hydrothermal method to synthesize a composite known as C@MoS_2, where 2D MoS_2 nanosheets are grown on carbon spheres. While C@MoS_2 showed improved electrochemical performance, challenges such as direct contact between MoS_2 and the electrolyte, as well as delamination of MoS_2 from the carbon substrate during expansion and shrinkage cycles, limited its cycle life to only 50 cycles. Further improvements are needed to address these issues and enhance the long-term stability of the composite.

To address this, researchers have explored novel approaches. One such approach involved fabricating MoS_2 in a yolk-shell structure, which acted as a barrier to volumetric expansion during lithium-ion insertion. In order to improve cyclic performance, researchers utilized a hydrothermal method to embed MoS_2 nanosheets into hollow mesoporous carbon spheres, creating MoS_2@C structures. The resulting electrode composed of hollow MoS_2@C demonstrated a remarkable reversible capacity of 962 mA h g^{-1} at a current density of 1 A g^{-1} even after 1000 cycles [132]. This approach showcases the potential of MoS_2@C structures for enhancing the long-term stability and electrochemical performance of energy storage devices. Another innovative strategy was reported by Hang et al., who epitaxially grew MoS_2 nano thorns on carbon nanotube backbones (MoS_2@CNT) using chemical vapor deposition (CVD) and subsequently layered this composite with a thin carbon shell, resulting in (CNT@MoS_2)@C.

Carbon nanotubes play a vital role in MoS_2 composites by providing efficient conductive pathways for electron transfer and preventing the delamination of MoS_2 due to strong C—S bonds. This synergistic effect leads to a large specific capacity of approximately 980 mA h g^{-1} after 200 cycles. Shen and colleagues demonstrated the growth of honeycomb-like MoS_2 on a 3D graphene layer foam, known as HC-MoS_2@GF, which exhibited a capacity of 1100 mA h g^{-1} with a capacity retention rate of 99 % after 40 cycles at a current density of 200 m A g^{-1}.

To further enhance the lithium insertion performance of MoS_2, additional electroactive materials such as metal sulfides and MXene have been incorporated. In a study conducted by Chen et al., they demonstrated the synthesis of MoS_2-on-MXene heterostructures by sulfidating $Mo_2TiC_2T_x$ MXene for Li incorporation. The incorporation of MXene in the heterostructures provided benefits such as enhanced electronic conductivity of MoS_2 and improved adsorption of Li and polysulfides. As a result, these heterostructures exhibited improved Coulombic efficiency and cyclic performance compared to pure MoS_2 [133]. Teng et al. achieved vertical growth of MoS_2 nanosheets on graphene sheets via a simple and scalable hydrothermal method. The formation of C-O-Mo bonds between MoS_2 and graphene facilitated electron transport and improved the structural stability of the electrode.

Liu et al. developed a sandwich structure composed of C-TiO_2@MoS_2 mixed nanosheets. This unique structure demonstrated a significantly improved specific capacity of 805.3 mA h g^{-1}, which is approximately 8.7 times higher than that of pristine MoS_2. These impressive results were obtained after 100 cycles at a current density of 100 mA g^{-1}. However, it is worth noting that the combination of carbon and MoS_2 often requires additional processes such as high-temperature carbonization, which may result in the formation of carbides.

Moreover, the limited energy storage capacity of carbon materials can hinder the overall specific capacity of MoS_2. Additionally, the unique hollow structure of the MoS_2/SnS hybrid composite offers several advantages for battery applications: **1)** The hollow structure provides a large number of active sites and short diffusion pathways for Li^+ ions, resulting in high capacity and excellent rate performance. **2)** The integration of MoS_2 and SnS facilitates lithium-ion diffusion by reducing the energy barrier for diffusion, as supported by density functional theory calculations (DFT), thereby contributing to the high-rate performance. **3)** The covalent bonding between MoS_2 nanosheets and SnS nanodots enhances the structural stability during lithiation/delithiation cycles, ensuring a stable framework. Moreover, this bonding promotes direct electron transfer within the composite material. These unique characteristics and synergistic effects of the MoS_2/SnS hollow structure composite hold great promise for improving the performance of lithium-ion batteries. Table 4 lists examples of MoS_2 usage as an anode in Li-ion applications.

Gu et al. [134] investigated the electrochemical performance of two-layer MoS_2@C_3N and three-layer C_3N@MoS_2@C_3N heterostructures as negative electrode materials in lithium-ion batteries (LIBs). They discovered that the diffusion barrier for Li^+ ions on the MoS_2@C_3N interlayer along specific paths ($T_{i\text{-}Mo} \rightarrow T_{i\text{-}Mo}$; $T_{i\text{-}Mo} \rightarrow H_{i\text{-}MoS} \rightarrow T_{i\text{-}Mo}$), was 0.28 eV, which is lower than the actual diffusion barrier exhibited by MoS_2 or C_3N alone (Fig. 6(c)). This reduced diffusion energy in the MoS_2@C_3N heterostructure facilitates rapid Li-ion mobility through different diffusion paths, benefiting from the synergistic effect of MoS_2 and C_3N (Fig. 6(a–c)) [134]. The two-layer MoS_2@C_3N heterostructure demonstrated a theoretical specific capacitance of 742.86 mA h g^{-1} at a mild open-circuit voltage of 0.17 V. On the other hand, the three-layer heterostructure of C_3N@MoS_2@C_3N exhibited enhanced Li-ion adsorption and excellent cycling stability, with a theoretical capacity of 813.60 mA h g^{-1} (Fig. 6(d, e)) [134]. These findings emphasize the potential of MoS_2@C_3N heterostructures as promising high-performance negative electrode materials for advanced LIBs.

Comparing the theoretical specific capacity of MoS_2@ C_3N heterostructure (~742.86 mA h g^{-1}) with other MoS_2-based and various heterostructures, it can be observed that MoS_2@ C_3N exhibits a significantly higher capacity (Fig. 6(f)). For instance, MoS_2@Ti_2CO_2 (~447 mA h g^{-1}) [135], MoS_2@ borophene (~539 mA h g^{-1}) [136], MoS_2@ VS_2 (~584 mA h g^{-1}) [137], Ti_2CO_2@graphene (~350 mA h g^{-1}) [138], MoSSe@ graphene (560 mA h g^{-1}) [139], and blue-P@ graphene heterostructures (~569 mA h g^{-1}) [140] possess lower specific capacities. The diffusion barriers for Li^+ ions on the MoS_2@ C_3N heterostructure are ~0.28 eV, which is comparable to that of the C_3N-graphene heterostructure (~0.28 eV) [141]. However, it is lower than the diffusion barriers of Ti_2CO_2@ graphene (~0.3 eV) [142], MoS_2@$TiCO_2$ (~0.57 eV) [135], MoS_2@B (~0.3 eV) [136], and MoS_2@ graphene (0.29 eV) [143]. On the other hand, it is higher than the diffusion barriers of C_3N/P (0.09 eV) [134], P@ graphene (~0.12 eV) [140], blue-P@ graphene (~0.13 eV) [140], MoSSe@ graphene (~0.17 eV) [145], and MoS_2@ VS_2 (~0.24 eV) [137] heterostructures. These findings demonstrate the favorable electrochemical properties and potential of the MoS_2@C_3N heterostructure as an anode material for lithium-ion batteries [134].

8. MXene as an anode material for LIBs

A novel type of two-dimensional graphene material called Ti_3C_2 MXene has emerged as an innovative discovery. In 2011, Barsoum's team first discovered the rapid synthesis of 2D layered transition metal carbides or carbonitrides known as MXene. The precursor of MXene is a three-layered composite denoted by the chemical formula MAX and $M_{n+1}AX_n$. The value of 'n' varies and represents different hexagonal layer structures, including $n = 1$, 2, and 3. The MAX segments can be categorized into three structural forms: 211, 312, and 413. The M layers consist of transition metal elements such as V, Ti, Cr, Mo, Nb, Zr, and Hf, Ta, while the A layers consist of various III/IV group elements, including S, P, Si, Al, Ga, As, Cd, In, Ge, Sn, Pb, and Tl. The X layers contain elements such as C and N [173]. The layered structure of MXene demonstrates remarkable stability during repetitive cycles of Li^+ lithiation and

Table 4
Some recorded MoS_2 as an anode for the Li-ion application.

No	Anode material	Synthesis methods	Specific capacity (mA h g ^{1}) and cyclic stability (A g ^{1})	Ref
1	Vertically aligned metallic MoS_2	Hydrothermal	1100 mA h g ^{1} @ 5 A/g, 589 mA h g ^{1} after 350 cycles	[132]
2	Metallic MoS_2 nanotubes	Solvothermal	1150 mA h g ^{1} @ 5C after 350 cycles, 150 mA h g ^{1} @ 20C	[133]
3	MoS_2 nanosheets		1409 mA h g ^{1} @ 0.1 A/g, 1230 mA h g ^{1} after 250 cycles	[134]
4	MoS_2@C/rGO	Hydrothermal synthesis	1164 mA h g ^{1}@ 0.2C	[135]
5	2D-MoS_2 nanowalls	Hydrothermal	880 mA h g ^{1} @ 0.1 after 50 cycles	[136]
6	Hierarchical MoS_2 tubular structures	Hydrothermal	1320 mA h g ^{1} @ 0.1 A/g	[137]
7	MoS_2@C	Hydrothermal	1119 mA h g ^{1} @ 0.1C after 100 cycles	[138]
8	MoS_2/C hybrid	In situ LT (20 °C)	854.3 mA h g ^{1} @ 0.1C	[139]
9	MoS_2NTs	In-situ grown, wet etching	1253 mA h g ^{1} @ 0.2C after 150 cycles	[140]
10	CNT/MoS_2 tubular nanohybrids	Electrospinning and carbonization	800 mA h g ^{1} 5C after 1000 cycles, 670 mA h g ^{1} @ 10C	[141]
11	MoS_2 hollow nanospheres	Solvothermal and sulfidation	1100 mA h g ^{1} @ 0.5C after 100 cycles	[142]
12	MoS_2/biocarbon	Biocarbon based template method	1129 mA h g ^{1}at 0.1 after 100 cycles	[143]
13	Bowl-like C@MoS_2 hybrid	Hydrothermal, etching	798 mA h g ^{1} @ 0.1 after 1000 cycles	[144]
14	MoS_2/graphene nanosheets	Solid-state pan-milling	654 mA h g ^{1} @ 0.2C after 150 cycles	[145]
15	MoS_2-on-Mxene	Hydrothermal, heat reaction	509 mA h g ^{1} @ 0.1 after 100 cycles	[146]
16	MoS_2-in-Ti_3C_2 hybrids	By confined reaction	906 mA h g ^{1} @ 0.1C	[147]
17	MoS_2/Ti_3C_2-MXene@C	Hydrothermal	1200 mA h g ^{1} @ 1C after 700 cycles	[148]
18	ordered-mesoporous-carbon/MoS_2	Self-assembly process	1400 mA h g ^{1} @ 0.1, 400 mA h g ^{1} at 10C after 300 cycles	[149]
19	MCC-G or MoS_2/$CoMo_2S_4$/Co_3S_4- rGO	Hydrothermal synthesis	770 mA h g ^{1} @ 0.2C	[150]
20	NCMTs@A-MoS_2	By carbonization	544 mA h g ^{1} @ 1C after 1000 cycles	[147]
21	MoO_2@few-layered MoS_2		533 mA h g ^{1} @ 0.5 after 350 cycles	[148]
22	MoO_2@MoS_2		1000 mA h g ^{1} @ 0.1C	[149]

Table 4 (*continued*)

No	Anode material	Synthesis methods	Specific capacity (mA h g ^{1}) and cyclic stability (A g ^{1})	Ref
23	EG/MoS_2	Hydrothermal	1250 mA h g ^{1} @ 1C after 150 cycles	[150]
24	GF@CNT@MoS_2		506 mA h g ^{1} @ 0.2 after 200 cycles	[151]
25	MoS_2/RGO	Hydrothermal	896 mA h g ^{1} @ 0.05C after 50 cycles	[152]
26	MoS_2/GNS	Hydrothermal	940 mA h g ^{1} @ 0.1C after 100 cycles	[153]
27	MoS_2/graphene hybrid	In situ mechanical peeling	553 mA h g ^{1} @ 0.25 after 100 cycles	[154]
28	MoS_2-MCNT hybrids	Hydrothermal	1090 mA h g ^{1} @ 0.1 after 30 cycles	[155]
29	Yolk-shell MoS_2 nano spheres	–	1010 mA h g ^{1} @ 1C after 200 cycles	[156]
30	yolk-shell MoS_2@C	Hydrothermal method	962 mA h g ^{1} @ 1C after 1000 cycles	[157]
31	MoS_2/SnS HSs	Covalent assembly strategy	988 mA h g ^{1} @ 0.2C, 643 at 5C	[158]
32	SnS/MoS_2-C	Hydrothermal	989 mA h g ^{1} @ 0.2C after 60 cycles	[159]
33	MoS_2@SnO_2-SnS/C nanosheets	Hydrothermal	852 mA h g ^{1} @ 0.2C after 100 cycles	[160]
34	SnO_2-SnS/C nanosheets	–	1006 mA h g ^{1} @ 0.2 A/g, 637 mA h g ^{1}after 500 cycles	[161]
35	MoS_2/ZnS/C	in situ strategy	961.9 mA h g ^{1} @ 0.1 after 100 cycles	[162]
36	Hollow Ni—Co skeleton@ MoS_2/MoO_3	Hydrothermal reaction	1720.6 mA h g ^{1} @ 0.2C after 317 cycles	[163]
37	Hierarchical MoS_2 nanotubes	Solvothermal	839 mA h g ^{1} @ 0.1 after 50 cycles	[164]
38	Core-shell TiO_2 @MoS_2	Hydrothermal reaction	467 mA h g ^{1} @ 0.1C	[165]
39	TiO_2@Carbon@MoS_2	Hydrothermal reaction	770 ma h g ^{1} @ 0.2c after 200 cycles	[166]
40	TiO_2/NC-MoS_2	Hydrothermal reaction and annealing treatment.	629.9 ma h g ^{1} @ 0.1 after 200 cycles	[167]
41	TiO_2/C/MoS_2 microspheres	Hydrothermal reaction	621 ma h g ^{1} @ 0.1c	[168]
42	V_4C_3-MXene/MoS_2/C	Etching, hydrothermal reaction	622.6 mA h g ^{1} @ 1C after 450 cycles	[169]
43	C_3N_5/MoS_2 hybrid	In situ polymerization	193 mA h g ^{1} @ 0.054C	[170]
44	Fe_3O_4/MoS_2 composites	Hydrothermal method	1033 mA h g ^{1} @ 0.5C after 1180 cycles 224 mA h g ^{1} @ 10C	[171]
45	Co_9S_8@MoS_2	Sol-gel method	1298 mA h g ^{1} @ 1 A/g, 1048	[172]

(*continued on next page*)

Table 4 (*continued*)

No	Anode material	Synthesis methods	Specific capacity (mA h g ^{1}) and cyclic stability (A g ^{1})	Ref
46	Co_3S_4@C@MoS_2	Solvothermal	mA h g ^{1} after 300 cycles 672.6 mA h g ^{1} after 500 cycles	[173]

de-lithiation. MXene has shown promising applications in lithium-ion batteries, hydrogen storage, membrane separation, supercapacitors, photocatalysis, and Li—S batteries.

The Ti_3C_2Tx hydrogel demonstrates exceptional photocatalytic performance due to its interconnected porous structure. The Simon and Gogotsi labs conducted research on MXene from 2012 to 2013, exploring its application as an anode material in lithium-ion batteries. The Ti_2CTx variant exhibited a tentative gravimetric capacity of 160 mA h g ^{1} for Li intercalation, which was 1.5 times higher than Ti_3C_2Tx (110 mA h g ^{1}) [174]. MXene, with its conductive nature and large interlayer spacing (0.7 to 1.1 nm), shows great potential for Li^+ ion storage. The lithium loading in MXene electrodes is influenced by various structural factors, including surface functional groups, chemical components, porous structures, and doped atoms. The presence of surface functional groups such as —F or -OH in Ti_3C_2-based electrodes can hinder Li^+ storage efficiency by impeding Li^+ transportation [175]. Optimal selection and quantity of functional groups can enhance the lithium storage performance. Furthermore, the surface functional groups present on MXenes offer additional sites for lithium storage, thereby making pure MXenes highly promising for application as anode materials in

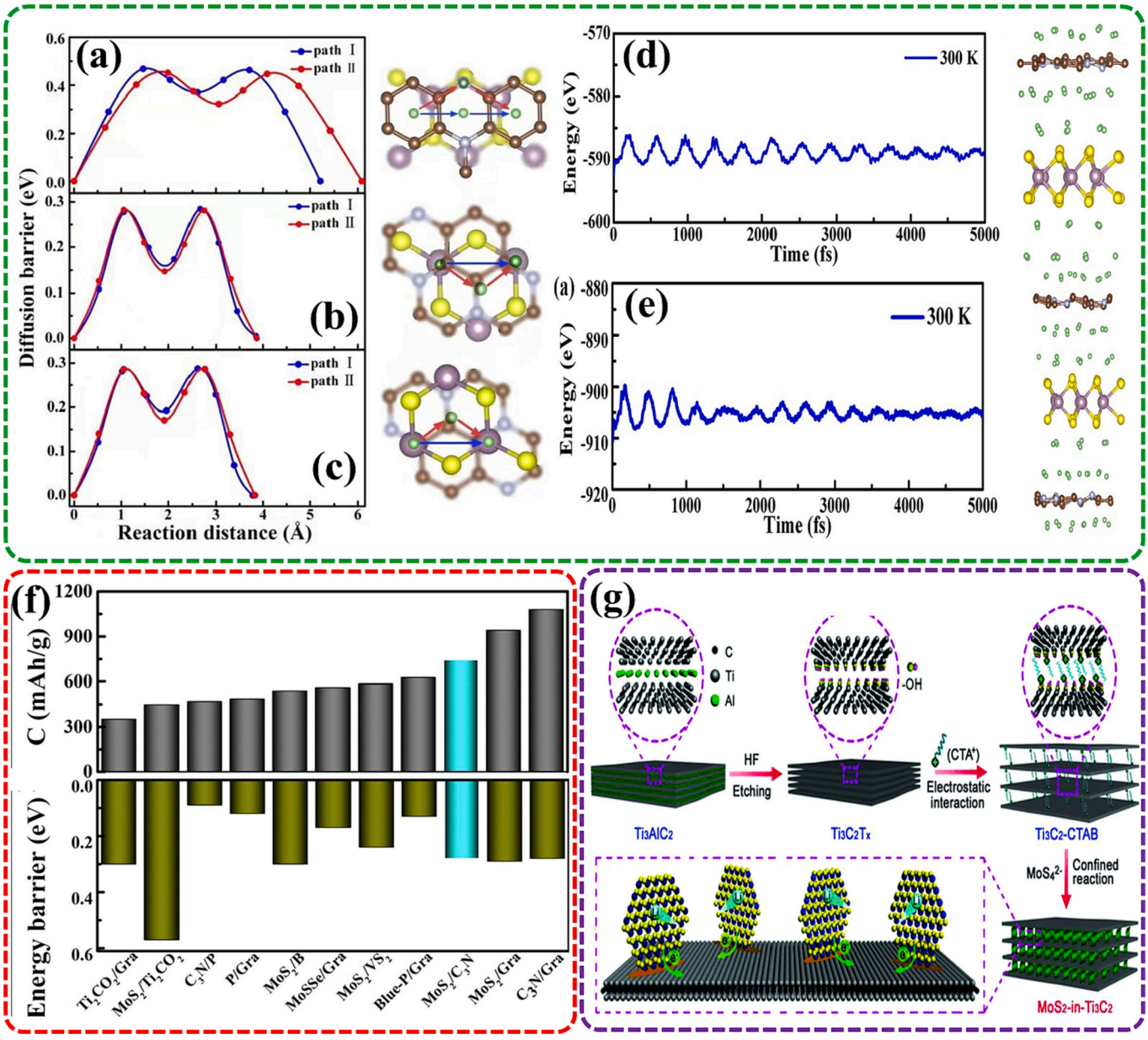

Fig. 6. Li-migration energy profiles and paths in different scenarios: (a); outside C3N, (b); middle layer of the MoS_2/C_3N heterostructure, and (c); outside MoS_2. It also includes the results of AIMD simulations and a side view of the total energy variation of $Li_{4.5}/MoS_2/Li_{5.25}/C_3N/Li_3$ at 300 K after 5 ps (d); The corresponding prints and energy fluctuations from AIMD simulations after 5 ps are shown in (e) [134]; The theoretical energy storage capacity and diffusion barrier of Li ions on various heterostructures used as anode materials for LIBs [64,134–139,141,144] (f). Illustrating the fabrication process of the MoS_2-in-Ti_3C_2 superstructure (g).

lithium-ion batteries (LIBs). LIBs typically operate within a potential-voltage window of 0.5–1.5 V in comparison to the Li/Li^+ reference electrode [176,177].

Barmann et al. [84] conducted a study to investigate the effect of post-treatment on the electrochemical performance of $Ti_3C_2T_x$ MXenes. The researchers prepared multiple layers of $Ti_3C_2T_x$ MXenes by selectively etching the $Ti_3C_2T_x$ MAX phase using a LiF/HCl mixture. Analysis of the PXRD patterns revealed that the samples treated with HCl and LiOH exhibited lower angle (002) peaks, indicating an increased interlayer spacing and the formation of layered $Ti_3C_2T_x$. The results from Brunner-Emmett-Teller theory (BET) showed that the specific surface area (SSA) of the HCl-treated $Ti_3C_2T_x$ decreased from 30.1 m2/g to 20.1 m^2/g after LiOH treatment. Electrochemical characterization demonstrated that the HCl-treated $Ti_3C_2T_x$ exhibited superior rate performance compared to other MXenes, as mentioned earlier. Specifically, at a high discharge rate of 5 A/g, the capacity values of the untreated $Ti_3C_2T_x$, HCl-treated $Ti_3C_2T_x$, and LiOH-treated $Ti_3C_2T_x$ samples were 131 mA h g^{-1}, 155 mA h g^{-1}, and 174 mA h g^{-1}, respectively (Fig. 7(d)). The notable improvement in the rate performance of the HCl-treated $Ti_3C_2T_x$ can be attributed to the efficient removal of impurities from LiF. In contrast, the LiOH-treated. Table 5 presents examples of Mexene used as an anode for Li-ion battery applications.

In terms of long-term stability, the LiOH-treated $Ti_3C_2T_x$ exhibited the best performance among the three samples at the investigated rates. At a current density of 0.5 A g^{-1}, all three samples showed activation behavior and increased capacity after 200 cycles. After 1000 cycles, the capacitance values of the pristine $Ti_3C_2T_x$, acid-treated $Ti_3C_2T_x$, and LiOH-treated $Ti_3C_2T_x$ samples were 320 mA h g^{-1}, 332 mA h g^{-1}, and 387 mA h g^{-1}, respectively, as depicted in Fig. 7(e). This trend was also observed at a higher current density of 5.0 A/g. The higher capacitance value of the LiOH-treated $Ti_3C_2T_x$ can be attributed to the co-intercalation of carbonate from the electrolyte into the layers of the MXene. The presence of Li ions in the few-layer $Ti_3C_2T_x$ MXene plays a crucial role in facilitating the intercalation of solvents from the electrolyte, thus influencing the capacity of the MXenes.

The introduction of heteroatoms in material structures has emerged as a powerful strategy for optimizing the bandgap and surface properties of MXenes family. For instance, $Mo_2TiC_2T_x$, with Mo atoms on the surface of MXene, exhibits a high capacity of 269 mAh/g at a current density of 0.1 A/g. Chen et al. conducted a study where they synthesized Mo-based 2D MoS_2-on-MXene heterostructures through in situ sulfurization of Mo_2TiC_2Tx MXene. Computational analysis reveals that these heterostructures exhibit metallic properties, and the insertion of MX enhances the adsorption of Li and Li_2S during intercalation and transformation reactions, as depicted in Fig. 7(a–c).

Incorporating Co^{2+} ions into V_2C MXene using a similar approach resulted in the formation of V-O-Co bonds, which increased the interlayer distance by 9.52 Å. This modified MXene, known as Co^{2+}-loaded V_2C MXene, exhibited excellent electrochemical performance, with a capacity of 1117.3 mA h g^{-1} at a current density of 0.1 A g^{-1} and an impressive cycle life of over 15,000 cycles. Despite these advancements, further investigation is needed to explore the introduction of other heteroatoms and adapt the porous structure to enhance ion diffusion within the electrode.

By developing such electrodes, it may be possible to eliminate the reliance on metal-based current collectors, conductive carbon-based additives, and polymer-based binders, leading to significant improvements in the energy density of lithium-ion batteries (LIBs). In a specific study, silver nanoparticles were uniformly deposited on $Ti_3C_2T_x$ nanosheets by reducing $AgNO_3$ in the MXene mixture.

Another positive approach involves the insertion of Sn nanoparticles into the MXene matrix through a facilitated PVP-assisted liquid-phase absorption process to prepare PVP-Sn(IV)@Ti_3C_2 hybrid packs. These hybrids exhibited a high reversible capacity of 1375 mAh/cm^2. Regarding the fabrication of MXenes, the initial MXene, Ti_3C_2, was obtained by selectively etching the precursor Ti_3AlC_2 phase in hydrofluoric acid (HF) solution. However, due to the toxic nature of HF, an alternative approach utilizing LiF salt as a precursor was introduced, which has gained significant research attention in MXenes since its development in 2014 [176]. Additionally, the incorporation of rare earth fluorides such as LaF_3 and CeF_3 can effectively prevent the high potential oxidation breakdown of the electrolyte and reduce cell polarization and separation.

Zhou et al. conducted a study to investigate $V_4C_3T_x$ MXenes synthesized by HF treatment of ball-milled and non-ball-milled V_4AlC_3 MAX phases [178179]. The HF treatment of ball-milled V_4AlC_3 resulted in smaller particle sizes compared to MXene derived from non-ball-milled V_4AlC_3. The study presented TEM images, galvanostatic charge/discharge curves, cycle performance, and rate performance of the $V_4C_3T_x$ samples, as depicted in Fig. 7(f, g). The TEM images revealed that ball milling of V_4AlC_3 led to the formation of $V_4C_3T_x$ with a larger interlayer spacing. The electrochemical results demonstrated that the ball-milling treatment significantly enhanced the electrochemical performance of $V_4C_3T_x$ MXene. Moreover, the specific capacity of $V_4C_3T_x$ obtained from ball-milled V_4AlC_3 was 225 mA h g^{-1} at a current density of 0.1 mA g^{-1}, while the capacity of $V_4C_3T_x$ derived from non-ball-milled V_4AlC_3 decreased to 185 mA h g^{-1} after 300 cycles, as shown in Fig. 7(h). Interestingly, both $V_4C_3T_x$ samples exhibited a similar activation process to that of $Nb_4C_3T_x$, suggesting that this electrochemical activation is unique to the structure of Nb/$V_4C_3T_x$ and likely involves a transition from fluorine-rich (—F) to oxygen-rich (—O) during the cycling process of the battery.

Niobium (Nb)-based MXenes have emerged as promising anode materials for lithium-ion batteries (LIBs), displaying superior reversible capacities compared to titanium (Ti)-based MXenes. For instance, Nb_2CT_x has demonstrated an excellent capacity exceeding 542 mA h g^{-1}, which is the highest reported value among $Ti_3C_2T_x$ MXenes (320 mA h g^{-1}) [179,180]. Therefore, it is crucial to review the significant studies focused on the lithium-ion storage capacity of Nb-based anodes in LIBs. Hu et al. [181,182] conducted research on the lithium-ion storage capacity of $Nb_4C_3T_x$ MXene. At a current density of 0.1 A g^{-1}, $Nb_4C_3T_x$ exhibited an initial discharge capacity of 546 mA h g^{-1} and an initial coulombic efficiency (ICE) of 60.9 %. Fig. 7 illustrates the electrochemical performance of Nb_2CT_x. Notably, the cyclic performance revealed an activation phenomenon in $Nb_4C_3T_x$ MXene. At a current density of 0.1 A g^{-1}, the capacity of Nb4C3Tx increased from 116 mA h g^{-1} to 320 mA h g^{-1} after 750 cycles. Detailed analysis using techniques such as powder X-ray diffraction (PXRD) and transmission electron microscopy (TEM) confirmed that the interlayer spacing of $Nb_4C_3T_x$ increased with each cycle, leading to a gradual increase in capacitance values throughout the process.

9. Into the depths: investigating the intercalation mechanism for Li storage

In the Ti_2C host, intercalation of a monolayer of Li atoms occurs between double layers of Ti atoms, while in the Ti_3C host, a monolayer of Li atoms is accommodated between triple layers of Ti atoms. The theoretical capacities of $Ti_2CO_2Li_2$ and $Ti_3C_2O_2Li_2$, determined through DFT calculations, were found to be 383 mA h g^{-1} and 268 mA h g^{-1}, respectively, indicating an intercalation mechanism for Li storage in Ti_2CT_x. Mashtalir et al. conducted research on intercalated Ti_3C_2 MXene flakes, demonstrating their potential as negative electrode materials for LIBs with high charging rate and stability [184].

Similarly, Naguib et al. synthesized a composite of vanadium carbide and niobium, which exhibited high rate capacity as LIB anodes [185]. The Nb_2CTx composite displayed a capacity of 180 mA h g^{-1} at the IC rate. Moreover, the utilization of a composite consisting of carbon nanotubes (CNTs) and Ti_3C_2 MXene flakes as an anode material demonstrated a specific capacity of 750 mA h g^{-1} [177]. In addition, the composite CTAB–Sn/Ti_3C_2 exhibited a remarkable capacity of 800 mA h g^{-1} at a normal current density of 0.1 A g^{-1}, surpassing the performance

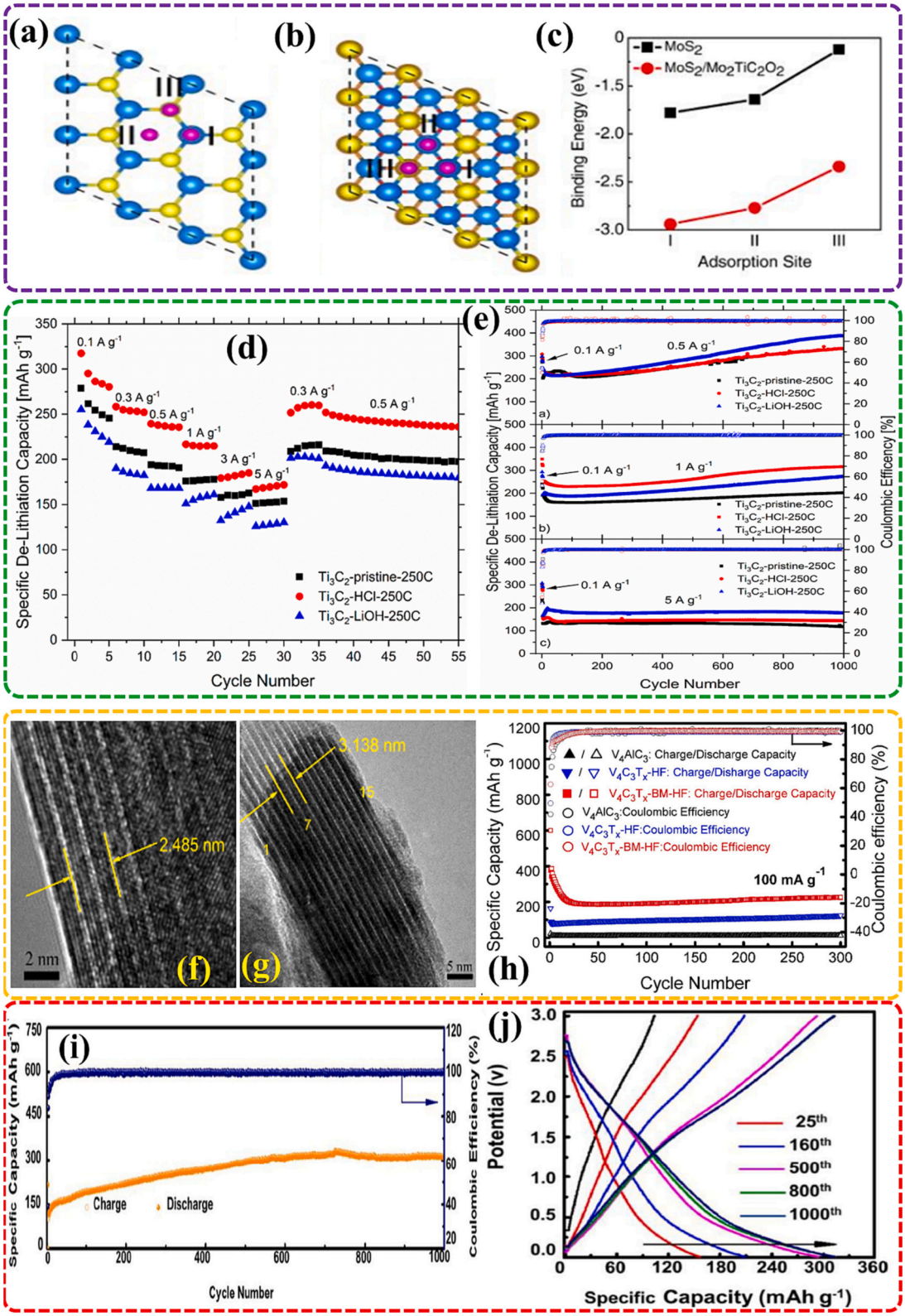

Fig. 7. The adsorption sites for Li on MoS_2 and $MoS_2/Mo_2TiC_2O_2$, as well as their respective binding energies, were investigated (a–c) [177,178]; The specific lithiation and delithiation capacities of $Ti_3C_2T_x$ materials (Ti_3C_2-HCl-250 °C, Ti_3C_2-LiOH-250 °C, and Ti_3C_2-pristine-250 °C) were evaluated in $Ti_3C_2T_x$||Li metal batteries at different specific current values (d, e) [182]. The morphology of $V_4C_3T_x$ prepared by different methods such as HF treatment of non-ball-milled V_4AlC_3, (f); $V_4C_3T_x$ by HF treatment of non-ball-milled V_4AlC_3, (g); were examined, along with cyclic performance at a current density of 0.1 A g^{-1} (h) [183]. Furthermore, the electrochemical performance of niobium $V_4C_3T_x$ (i); was investigated, including long-term cycling performance at a current density of 1 A g^{-1} (j); and charge-discharge capacity curves at different cycle numbers (k) [181].

Table 5
Some listed Mexene as Anode for Li-Ion batteries application.

No	Anode material	Synthesis methods	Specific capacity (mA h g ^{1}) and cyclic stability (A g ^{1})	Ref
1	Ti_2CT_x	–	225 at 0.04 after 80 Cycles	[189]
2	Ti_3CNT_x	–	300 at 0.5 after 1000 cycles	[190]
3	$Ti_3C_2T_x$	Exfoliation process	203 at 0.2C after 500 cycles	[191]
4	CNTs@Ti_3C_2		430 at 1C after 300 cycles	[192]
5	CNT/$Ti_3C_2T_x$	vacuum filtration.	1250 at 0.5C after 100 cycle	[193]
6	Ti_2CNT_x		310 at 0.5 after 1000 cycles	[194]
7	Ti_3C_2/CNF	Low temperature exfoliation, Vacuum assisted filtration	320 at 1C	[195]
8	rGO/$Ti_3C_2T_x$ film		221 at 0.05C after 275 cycles	[196]
9	Ti_3C_2/ Si@SiO_x@C	Sol-gel process	1444 at 0.5C, 510 at 10C after 1000 cycles	[197]
10	silicon/$Ti_3C_2T_x$	Etching, electrostatic self-assembly	1067.6 at 0.3 after 100 cycles	[198]
11	$Ti_3C_2T_x$ @LaF_3	Solid-phase sintering	340	[199]
12	Si@ $Ti_3C_2T_x$		188 at 0.2 after 150 cycles	[200]
13	nSi/Ti_3C_2Tx		2100 at 1.5C, 1280 after 275 cycles	[201]
14	nSi/Ti_3CNT_x		1600 at 1.5C, 1100 after 70 cycles	[202]
15	N $Ti_3C_2T_x$/P	Hf Etching process	801 at 0.51040 cycles	[203]
16	$Nb_4C_3T_x$	Delamination with TMAOH	380 at 0.1after 100 cycles	[203]
17	Nb_2CT_x@CNT paper		400 at 0.5C	[204]
18	Nb_2O_5/Nb_4C_3Tx	One-step oxidation —in flowing CO_2 at 850 °C	208 at 0.25 after 400 cycles	[205]
19	Nb_2O_5/$Nb_4C_3T_x$	Template free one-pot method	280 at 0.05C	[206]
20	Nb_2CTx/CNT	Etching	460 at 0.5C after 100 cycles	[207]
21	N-Nb_2CT_x	Hydrothermal reaction	360 at 0.2	[208]
22	Fe_3O_4@ $Ti_3C_2T_x$	Solvothermal process.	747 at 1C after 1000 cycles	[209]
23	PVP–Sn (IV)/ Ti_3C_2	(PVP) assisted liquid-phase immersion process	1626 at 0.5C and 544 after 200 cycles	[210]
24	Ti_3C_2Tx/ $NiCo_2O_4$	Hydrothermal method and subsequent annealing process	1330 at 0.1C after 100 cycles	[211]
25	$Mo_2TiC_2T_x$ nanosheet	Electrochemical exfoliation	265 0.1C	[212]
26	SnO_2/$Ti_3C_2T_x$	Electrostatic self-assembly	655.2 at 0.1C	[213]
27	SnO_2/Ti_3C_2	Hydrothermal reaction and a further calcination process.	916 at 0.5C and 843 after 50 cycles	[214]
28	SnO_2/Ti_3C_2/ HfO_2	Wet etching methods	843 at 0.5 after 50 cycles	[215]
29	MXene/ Si@SiO_x@ C		1674 at 0.2C	[216]
30	HfO_2-coated SnO_2/MXene	Atomic layer deposition.	260 at 0.5C	[217]
31	MoS_2/Ti_3C_2	Hydrothermal method	1210 at 20C and 580 after 3000 cycles	[218]
32	MoS_2/Ti_3C_2@C	Hydrothermal method	1130 at 0.2C	[219]
33	MoS_2/ Mo_2TiC_2Tx	In situ sulfidation	548 at 0.05C after 100 cycles	[220]
34	Mo_2C/CNT	Scalable spray-drying	560 at 0.4C after 70 cycles	[221]
35	$Ti_3C_2T_x$/Co_3O_4	Ultrasound treatment	1200 at 0.1C after 100 cycles	[221]
36	SnO_x@Ti_3C_2	Microwave-assisted method	450 at 0.2C after 250 cycles	[222]
37	SnO_2/Ti_3C_2	Hydrothermal method	1030 at 0.3C and 360 after 200 cycles	[223]
38	SnO_2 nanowires/Ti_3C_2	Solvothermal	530 at 1C after 500 cycles	[224]
39	SnO_2/Ti_3C_2Tx	Microwave-assisted method	400 at 0.1C and 360 after 200 cycles	[225]
40	Ag/Ti_3C_2Tx	Chemical self-reduction	310 at 1C after 800 cycles	[226]
41	Ag/Ti_3C_2(OH) $0.8F_{1.2}$	Direct reduction of $AgNO_3$ aqueous solution	310 at 1C after 5000 cycles	[227]
42	Bi_2MoO_6/MXene	Soft chemical synthesis electrostatic assembling	692 at 0.1C after 200 cycles	[228]
43	TiO_2/Ti_2CTx	Hydrothermal partial oxidation of Ti3C2	389 at 0.1C after 70 cycles	[229]
44	TiO_2 nanorods/ Ti_3C_2	Hydrothermal oxidation	138 at 20C	[230]
45	TiO_2/Ti_3C_2Tx	Hydrothermal process	267 at 0.2C after 2000 cycles	[231]
46	$Na_{0.23}TiO_2$/ $Ti_3C_2T_x$		178 at 5C after 4000 cycles	[232]
47	BPQDs/Ti_3C_2	Low-temperature hydrothermal strategy,	520 at 10C after 2400 cycles	[233]
48	$LiMn_2O_4$/ Ti_3C_2Tx	Electrostatic self-assembly process.	114.1 at 1C	[234]
49	$Li_4Ti_5O_{12}$-Ti_3C_2Tx	High temperature calcination method	178 at 5C after 500 cycles	[235]

of pristine Ti_3C_2. These results suggest that Sn nanoparticle/Ti_3C_2 composites show similar performance to CTAB/Ti_3C_2 composites in terms of capacity and functionality.

Mashtalir et al. successfully increased the interlayer spacing of Ti_3C_2Tx, Ti_2CNTx, and TiNbCTX compounds through intercalation of urea, dimethyl sulfoxide (DMSO), and hydrazine monohydrate. DMSO was particularly effective in achieving wide-ranging delamination of Ti_3C_2Tx through sonication, resulting in a lower adsorption resistance. Mashtalir et al. provided evidence to support this hypothesis by observing the formation of a unique solid-electrolyte interphase (SEI) during the cyclic process, resulting in an increase in capacity. Additionally, Shen et al. demonstrated the successful plating of Li metal on porous 3D-printed $Ti_3C_2T_x$ substrates. Zhang et al. synthesized a composite material, N-doped Ti_3C_2@Si@SiO_x@C, using magnesia thermic reduction, carbonation, and the Stöber method. The large interlayer spacing in MXenes allows for contraction and expansion during cycling, facilitating the expansion of Si atoms. Remarkably, after 1000 cycles at a current density of 10C, the anode electrode swelled to 1.12 times its original thickness. In comparison, the commercial Si/C electrode swelled to 1.54 times its original thickness, leading to detachment from the current collector. Due to their low diffusion resistance, MXene-based anodes exhibit exceptional electrochemical performance, particularly at high currents [186]. Table 6 showcases recorded instances of B/P used as an anode for Li-ion battery applications.

The utilization of Fe_3O_4@Ti_2C_3 as an anode electrode for lithium batteries resulted in exceptional performance, with a remarkable capacity of approximately 747 mA h g ^{1} observed at 1C over the course of 1000 cycles [187]. Additionally, these electrode materials exhibited a substantial capacity of around 278 mA h g ^{1} even at a high rate of 5C, showcasing their capability to deliver energy rapidly [187]. In another

Table 6
Some recorded B/P as Anode for Li-Ion batteries application.

No	Anode material	Specific capacity (mA h g ^{1}) & cyclic stability (A g ^{1})	Ref
1	Borophene	929 mA h g ^{1}and 584 mA h g ^{1}	[242]
2	Borophane	504 mA h g ^{1}	[243]
3	h-borophene	5268 mA h g ^{1}	[244]
4	Black phosphene	315 mA h g ^{1}	[245]
5	C_3B	714 mA h g ^{1}	[246]
6	B_3S	1662 mA h g ^{1}	[247]
7	B_2S monolayer	1498 mA h g ^{1}	[248]
8	Mo_2B_2	251 mA h g ^{1}	[249]
9	borophene/boron nitride(B/BN)	1698 mA h g ^{1}	[250]
10	β_{12}-borophene	1984 mA h g-1	[251]
11	χ3-borophene	1240 mA h g ^{1}	[251]
12	BP monolayer,	1283 mA h g ^{1}	[252]
13	Planar B_7P_2 monolayer	3117 mA h g ^{1}	[253]
14	Triangular borophene	3306 mA h g ^{1}	[254]
15	flat borophene films	2040 mA h g ^{1}	[255]
16	Phosphorene	~433 mA h g ^{1}	[256]
17	Phosphorene ribbons	~541 mA h g ^{1}	[257]
18	C_3N/phosphorene	468.34 mA h g ^{1} @ 0.02 A g ^{1}	[258]
19	Phosphorene–graphene	1306.7 mA h g ^{1}@ 0.2C, ~1200 mA h g ^{1} after 800 cycles	[259]
20	Blue phosphorene/graphene	~485 mA h g ^{1}	[260]
21	Blue phosphorene/MS_2	~528.257 mA h g ^{1}	[261]
22	Hexagonal boron nitride/blue phosphorene	~801 mA h g ^{1}	[262]

study, Zhang et al. explored the potential of MXenes as conductive binders for viscous aqueous inks containing silicon materials. The MXenes were also employed as anode materials for lithium-ion batteries (LIBs) [188]. This approach demonstrated promising results, highlighting the suitability of MXenes as conductive binders in facilitating the effective integration of silicon materials into LIB electrodes [187] (Fig. 8).

10. Advancement in phosphorene, borophene as anode material for LIBs

Phosphorus is a two-dimensional material with a tunable bandgap. It possesses a stable ring structure, where each phosphorus atom is connected end-to-end with three other phosphorus atoms, similar to the arrangement of carbon atoms in graphene. Phosphorene shows great potential as an energy storage material, particularly for battery applications. However, there is currently limited literature available to fully validate its functionality as an electrochemical energy storage material.

Single-layer black phosphorus, also known as phosphorene, typically exhibits a folded honeycomb structure. The interlayer interaction between single layers of phosphorene in bulk black phosphorus is attributed to weak van der Waals forces. Mechanical stripping is commonly employed to synthesize black phosphorus.

Qiao et al. conducted a comprehensive investigation into the properties of black phosphorus (BP) using density functional theory (DFT) calculations. Their study conclusively confirmed that black phosphorus exhibits the characteristics of a P-type direct bandgap semiconductor. Through DFT calculations, they analyzed important properties such as carrier mobility, anisotropy, and bandgap of black phosphorus. The results revealed that the electronic mobility of black phosphorus is relatively lower than the N-type hole mobility. Furthermore, the positioning of the upper and middle valence band structures adjacent to the bottom of the energy band at the same K point provides further evidence of the semiconducting nature of black phosphorus [236].

Kulish et al. conducted first-principles calculations to investigate the impact of sodium ion concentration on the mechanical properties and electronic structure of black phosphorus. The results revealed a significant negative adsorption energy between individual phosphorus and sodium atoms, indicating a robust interaction between these two elements. The DFT calculations also predicted specific capacities of 865 mAh/g for sodium-treated phosphorus (NaP) and 433 mA h g ^{1} for Na_2P. Despite its high theoretical capacity, black phosphorus exhibits significant capacitance decay after the first cycle in the electrochemical mechanism, likely due to its poor electrical conductivity. The composite exhibited an impressive specific capacitance of 2168.8 mA h g ^{1} and demonstrated excellent cycle stability. Notably, even after 200 cycles, the specific capacitance remained within the range of 1677.3 mA h g ^{1}, highlighting its promising performance and potential for long-term use in energy storage applications [237].

Similar to phosphorene, borophene is another lightweight metallic two-dimensional material that shares analogies with graphene. It is composed of thin layers of boron and lacks the ability to form graphene-like structures due to its electron-deficient nature. Boron, as the fifth element in the periodic table, acts as an electron acceptor and forms bonds with semiconductors such as germanium and silicon.

According to Zhao et al. [238], borophene exhibits superconducting properties with a threshold temperature surpassing that of liquid hydrogen. It also possesses favorable adsorption energy capabilities in the range of 0.57–2.85 eV, as described by Yu et al. [239]. Yuan et al. [240] and Wang et al. [239] investigated monolayer Zr_2B_2, which

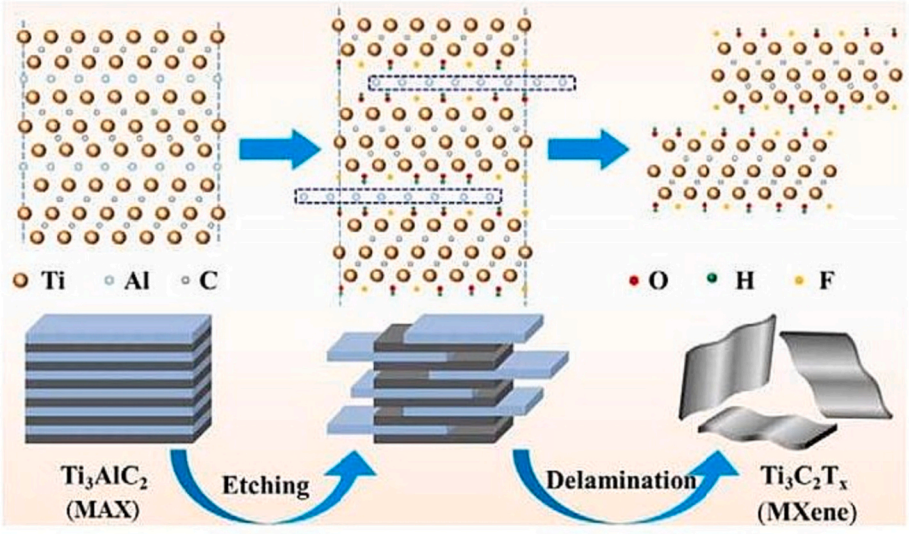

Fig. 8. Schematic process diagram to prepare Ti_3C_2Tx [187].

demonstrated a stable lithiation process and a high specific capacity of 526 mA h g^{-1}. The composite of Zr_2B_2 and lithium as an electrode exhibited an extremely low energy barrier (0.0017 eV) for lithium adsorption on the surface of mono-layer borophene. Jiang et al. [240] examined the anode capacities of borophene for lithium-ion batteries, revealing a specific energy of 1.12 eV and an adsorption capacity of 1860 mAh/g through ab-initio molecular dynamics simulation.

Mortazavi et al. [241] conducted an initial study on flat borophene, and different types of borophene, such as planar striped borophene (β_{12}-borophene) and χ3-borophene, have been explored as anode materials in lithium batteries. The exceptional lithium storage capacities of phosphorene and borophene have motivated further investigations on B—P binary monolayers. Recently, the fabrication of a composite B_7P_2 layer with similar topologies to borophene by incorporating the larger atomic radius of phosphorus and B_7 units from borophene has shown promising results as a high-performance negative electrode material for lithium-ion batteries.

In conclusion, the choice of a graphite or 2D anode depends on the specific requirements of the application, including energy density, rate capabilities and safety concerns. While graphite anodes are well established and have good cyclic stability, 2D materials offer the potential for increased capacity and improved rate ability, but with challenges in terms of synthesis, stability and safety. The aim of ongoing research is to overcome these challenges and unlock the full potential of both types of anode materials for advanced energy storage systems.

11. Conclusion and future perspectives

In this comprehensive review paper, we aim to provide an overview of the current research advancements in the utilization of two-dimensional (2D) materials for electrochemical energy storage technologies, with a particular focus on lithium-ion batteries (LIBs). The remarkable physiochemical properties exhibited by 2D materials have sparked significant interest in their potential applications in energy conversion and storage. The unique characteristics of 2D materials, including their large specific surface area, short diffusion path, favorable electrical conductivity, and exceptional electrochemical stability, make them highly attractive for energy storage applications. As a result, extensive research efforts have been dedicated to the study of 2D materials in recent years. In this paper, we have summarized the recent advancements in the field, with specific emphasis on prominent 2D materials such as graphene, WS_2, phosphorene, MoS_2, and MXene.

In conclusion, while 2D materials exhibit exceptional potential for revolutionizing electrochemical energy storage technologies, further research and development are necessary to overcome the remaining challenges and fully exploit their capabilities. Continued investigations into the synthesis, characterization, integration, and performance optimization of 2D materials will undoubtedly pave the way for their successful industrial commercialization in the future.

The future prospects of two-dimensional materials in energy storage and conversion are highly promising. As research in this field continues, several key areas of focus can be identified. Despite the significant progress made in understanding and utilizing 2D materials, there are still challenges that need to be addressed before effectively commercializing them for industrial applications.

Further research is required to delve deeper into the fundamental properties of these materials, optimize their synthesis and processing techniques, and explore their performance under real-world conditions. Scalability and cost-effectiveness of producing 2D materials at an industrial scale need to be considered. Compatibility and integration of 2D materials with existing battery architectures and electrolyte systems should be investigated to ensure seamless incorporation into practical energy storage devices. The development of efficient and reliable electrode architectures, tailored interfaces, and robust electrode-electrolyte interactions will be crucial for enhancing the overall performance and longevity of 2D-material-based energy storage systems.

Firstly, further exploration of novel two-dimensional materials with tailored properties will expand the range of options for anode materials, enabling better performance and energy storage capabilities. Optimizing synthesis, fabrication, and integration techniques is crucial for achieving scalable production and practical implementation of these materials in commercial devices. The stability and cycling performance of two-dimensional materials should be improved to ensure long-term reliability in energy storage systems. Moreover, the development of multifunctional two-dimensional materials that can simultaneously address multiple energy-related applications, such as catalysis and supercapacitors, holds great potential. Finally, addressing the environmental impact and sustainability aspects of these materials during production and disposal will be important for their widespread adoption in the future.

Declaration of competing interest

The authors declare that they have no known competing financial interests or personal relationships that could have appeared to influence the work reported in this paper.

Data availability

Data will be made available on request.

Acknowledgment

This work was supported by (i) Grant of the Comenius University Bratislava for Young Scientists (UK/24/2023). (ii) Slovak Research and Development Agency (APVV) through the project under contract No. APVV-21-0039, (iii) Scientific Grant Agency of the Slovak Ministry of Education, Sciences, Research and Sport (VEGA) through the project No. 1/0319/23.

References

[1] D. Larcher, J.M. Tarascon, Nat. Chem. 7 (2015) 19–29.
[2] Y. Lu, L. Yu, X.W. Lou, Inside Chem. 4 (2018) 972–996.
[3] M.B. Hanif, M. Motola, S. Rauf, C.J. Li, C.X. Li, Chem. Eng. J. 428 (2022) 132603.
[4] N. Tarasova, M.B. Hanif, N.K. Janjua, S. Anwar, M. Motola, D. Medvedev, Int. J. Hydrog. Energy (2023).
[5] M.B. Hanif, S. Rauf, Z. ul Abadeen, K. Khan, Z. Tayyab, S. Qayyum, M. Motola, Matter 6 (6) (2023) 1782–1830.
[6] M. Armand, J.-M. Tarascon, Building better batteries, Nature 451 (2008) 652–657.
[7] I. Shaheen, I. Hussain, T. Zahra, M.S. Javed, S.S.A. Shah, K. Khan, K. Zhang, J. Energy Storage 72 (2023) 108719.
[8] M. Hayat, Y. Zhou, M.Z.U. Shah, M.B. Hanif, H. Hou, U. Arif, R. Vadla, Chemosphere (2023) 139720.
[9] X. Xu, C.S. Rout, J. Yang, R. Cao, P. Oh, H.S. Shin, et al., J. Mater. Chem. 1 (2013) 14548.
[10] J. Liang, X.-Y. Yu, H. Zhou, H.B. Wu, S. Ding, X.W. Lou, Angew. Chem. Int. Ed. 53 (2014) 12803–12807.
[11] L. Suo, Y.-S. Hu, H. Li, M. Armand, L. Chen, Nat. Commun. 4 (2013) 1481.
[12] M. Idrees, S. Batool, Q. Zhuang, J. Kong, I. Seok, J. Zhang, et al., Ceram. Int. 45 (2019) 10572.
[13] M.N. Obrovac, L. Solid-State, Lett. 7 (2004) A93–A96.
[14] N.S. Choi, Z. Chen, S.A. Freunberger, X. Ji, Y.K. Sun, K. Amine, et al., Angew. Chem. Int. Ed. 51 (2012) 9994.
[15] L. Peng, Y. Zhu, D. Chen, R.S. Ruoff, G. Yu, Adv. Energy Mater. 6 (2016) 1600025–1600045.
[16] K.S. Novoselov, A.K. Geim, S.V. Morozov, D. Jiang, Y. Zhang, S.V. Dubonos, I. V. Grigorieva, A.A. Firsov, Science 306 (2004) 666–669.
[17] A. Sibari, A.E. Marjaoui, M. Lakhal, Z. Kerrami, A. Kara, et al., Sol. Energy Mater. Sol. Cells 180 (2018) 253–257.
[18] K. Khan, H. Xin, B. Fu, M.B. Hanif, P. Li, B.A. Beshiwork, M. Wu, J. Colloid Interface Sci. 642 (2023) 246–254.

[19] G.K. Thirunavukkarasu, M.B. Hanif, V. Liapun, K. Hensel, J. Kupčík, J. Lorincik, M. Motola, Mater. Res. Bull. 165 (2023) 112322.
[20] K. Khan, B. Fu, H. Xin, B.A. Beshiwork, M.B. Hanif, J. Wu, M. Wu, Ceram. Int. 49 (3) (2023) 4473–4481.
[21] M.B. Hanif, G.K. Thirunavukkarasu, V. Liapun, H. Makarov, M. Gregor, T. Roch, M. Motola, Nanoscale 14 (32) (2022) 11703–11709.
[22] M.B. Hanif, S. Rauf, M. Motola, Z.U.D. Babar, C.J. Li, C.X. Li, Mater. Res. Bull. 146 (2022) 111612.
[23] V. Liapun, M.B. Hanif, M. Sihor, X. Vislocka, S. Pandiaraj, V.K. Unnikrishnan, M. Motola, Chemosphere 337 (2023) 139397.
[24] L.F. Wan, J.T. Incorvati, K.R. Poeppelmeier, D. Prendergast, Chem.Mater. 28 (2016) 6900–6908.
[25] Q. Xue, Z.X. Pei, Y. Huang, M.S. Zhu, Z.J. Tang, H.F. Li, Y. Huang, N. Li, H. Y. Zhang, C.Y. Zhi, J. Mater, Chem. A 5 (2017) 20818–20823.
[26] K.W. Nam, H. Kim, J.H. Choi, J.W. Choi, Energy Environ. Sci. 12 (2019) 1999–2009.
[27] Z.L. Tao, L.N. Xu, X.L. Gou, J. Chen, H.T. Yuan, Chem. Commun. (2004) 2080–2081.
[28] Y.R. Wang, Z.T. Liu, C.X. Wang, X. Yi, R.P. Chen, L.B. Ma, Y. Hu, G.Y. Zhu, T. Chen, Z.X. Tie, J. Ma, J. Liu, Z. Jin, Adv. Mater. 30 (2018) 1802563.
[29] P. He, M. Yan, G. Zhang, R. Sun, L. Chen, Q. An, L. Mai, Adv. Energy Mater. 7 (2017) 1601920.
[30] B. Liu, T. Luo, G.Y. Mu, X.F. Wang, D. Chen, G.Z. Shen, ACS Nano 7 (2013) 8051–8058.
[31] L.M. Zhou, F.Y. Xiong, S.S. Tan, Q.Y. An, Z.Y. Wang, W. Yang, Z.L. Tao, Y. Yao, J. Chen, L.Q. Mai, Nano Energy 54 (2018) 360–366.
[32] Y. Liang, R. Feng, S. Yang, H. Ma, J. Liang, J. Chen, Adv. Mater. 23 (2011) 640–643.
[33] G.Z. Fang, Q.C. Wang, J. Zhou, Y.P. Lei, Z.X. Chen, Z.Q. Wang, A.Q. Pan, S. Q. Liang, ACS Nano 13 (2019) 5635–5645.
[34] M. Naguib, M. Kurtoglu, V. Presser, J. Lu, J.J. Niu, M. Heon, L. Hultman, Y. Gogotsi, M.W. Barsoum, Adv. Mater. 23 (2011) 4248–4253.
[35] A. Vahid Mohammadi, A. Hadjikhani, S. Shahbazmohamadi, M. Beidaghi, ACS Nano 11 (2017) 11135–11144.
[36] M. Naguib, O. Mashtalir, J. Carle, V. Presser, J. Lu, L. Hultman, Y. Gogotsi, M. W. Barsoum, ACS Nano 6 (2012) 1322–1331.
[37] M. Ghidiu, M. Naguib, C. Shi, O. Mashtalir, L.M. Pan, B. Zhang, J. Yang, Y. Gogotsi, S.J.L. Billinge, M.W. Barsoum, Chem. Commun. 50 (2014) 9517–9520.
[38] S. Manzeli, D. Ovchinnikov, D. Pasquier, O.V. Yazyev, A. Kis, Nat. Rev. Mater. 2 (2017) 17033.
[39] H.L. Zhuang, A.K. Singh, R.G. Hennig, Phys. Rev. B: Condens. Matter Mater. Phys. 87 (2013) 165415.
[40] A.K. Singh, R.G. Hennig, Appl. Phys. Lett. 105 (2014) 042103.
[41] H. Zhou, M. Zhao, X. Zhang, W. Dong, X. Wang, H. Bu, A. Wang, J. Phys. Condens. Matter 25 (2013) 395501.
[42] J.H. Yang, Y. Zhang, W.J. Yin, X. Gong, B.I. Yakobson, S.H. Wei, Nano Lett. 16 (2016) 1110–1117.
[43] Yan He, Libo Wang, Xiaolong Wang, Changjie Shen, Qianku Hu, Aiguo Zhou, Xuqing Liu, J. Mater. Sci. Mater. Electron. 31 (2020) 6735–6743.
[44] A.H. Khan, S. Ghosh, B. Pradhan, A. Dalui, L.K. Shrestha, S. Acharya, K. Ariga, Bull. Chem. Soc. Jpn. 90 (2017) 627–648.
[45] K.S. Novoselov, D. Jiang, F. Schedin, T.J. Booth, V.V. Khotkevich, S.V. Morozov, A.K. Geim, PNAS, USA 102 (2005) 10451–10453.
[46] H. Li, J. Wu, Z. Yin, H. Zhang, Acc. Chem. Res. 47 (2014) 1067–1075.
[47] A.S. Golub, Y.V. Zubavichus, Y.L. Slovokhotov, Y.N. Novikov, Russ. Chem. Rev. 72 (2003) 123–141.
[48] B. Anasori, Y. Xie, M. Beidaghi, J. Lu, B.C. Hosler, L. Hultman, P.R.C. Kent, Y. Gogotsi, M.W. Barsoum, ACS Nano 9 (2015) 9507–9516.
[49] S. Yang, P. Zhang, F. Wang, A.G. Ricciardulli, M.R. Lohe, P.W.M. Blom, X. Feng, Angew. Chem. Int. Ed. 57 (2018) 15491–15495.
[50] O. Mashtalir, M. Naguib, V.N. Mochalin, Y. Dall'Agnese, M. Heon, M.W. Barsoum, Y. Gogotsi, Nat. Commun. (2013) 4.
[51] O. Mashtalir, M.R. Lukatskaya, M.-Q. Zhao, M.W. Barsoum, Y. Gogotsi, Adv. Mater. 27 (2015) 3501–3506.
[52] M. Ghidiu, M.R. Lukatskaya, M.Q. Zhao, Y. Gogotsi, M.W. Barsoum, Nature 516 (2014) 78–81.
[53] Y. Yao, Z. Lin, Z. Li, X. Song, K.S. Moon, C.P. Wong, J. Mater. Chem. 22 (2012) 13494–13499.
[54] Z. Wu, B. Fang, A. Bonakdarpour, A. Sun, D.P. Wilkinson, D. Wang, Appl. Catal., B 125 (2012) 59–66.
[55] S. Eigler, M. Enzelberger-Heim, S. Grimm, P. Hofmann, W. Kroener, A. Geworski, C. Dotzer, M. Röckert, J. Xiao, C. Papp, O. Lytken, Adv. Mater. 25 (2013) 3583–3587.
[56] C. Tan, H. Zhang, Nat. Commun. 6 (2015) 7873.
[57] J. Bobnar, M. Lozinsek, G. Kapun, C. Njel, R. Dedryvère, B. Gènorio, R. Dominko, Energy Batt. Sci. Rep. 8 (2018) 1–10.
[58] W. Lei, S. Qin, D. Liu, D. Portehault, Z. Liu, Y. Chen, Chem. Commun. 49 (2013) 352–354.
[59] H. Sun, D. Hanlon, D.A. Dinh, J.B. Boland, A.E. Del Rio Castillo, C. Di Giovanni, A. Ansaldo, V. Pellegrini, J.N. Coleman, F. Bonaccorso, 2D Mater. 5 (2018) (No. 015024).
[60] X. Han, Y. Gong, K. Fu, X. He, G.T. Hitz, J. Dai, A. Pearse, B. Liu, H. Wang, G. Rubloff, Y. Mo, V. Thangadurai, E.D. Wachsman, L. Hu, Nat. Mater. 16 (2017) 572–579.
[61] S.B. Patil, H.J. Kim, H.K. Lim, S.M. Oh, J. Kim, J. Shin, H. Kim, J.W. Choi, S. J. Hwang, ACS Energy Lett. 3 (2018) 412–419.
[62] D.Y. Oh, Y.E. Choi, D.H. Kim, Y.G. Lee, B.S. Kim, J. Park, H. Sohn, Y.S. Jung, All-Solid- J. Mater. Chem. A 4 (2016) 10329–10335.
[63] S. Liu, X. Lu, J. Xie, G. Cao, T. Zhu, X. Zhao, ACS Appl. Mater. Interfaces 5 (2013) 1588–1595.
[64] X. Chen, Z. Kong, N. Li, X. Zhao, C. Sun, Phys. Chem. Chem. Phys. 18 (2016) 32937–32943, 2016.
[65] H. Lin, D.D. Yang, N. Lou, S.G. Zhu, H.Z. Li, Ceram. Int. 45 (2019) 1588–1594.
[66] A.H.C. Neto, F. Guinea, N.M.R. Peres, K.S. Novoselov, A.K. Geim, Rev. Mod. Phys. 81 (2009) 109.
[67] C.N.R. Rao, A.K. Sood, K.S. Subrahmanyam, A. Govindaraj, Angew. Chem. Int. Ed. 48 (2009) 7752.
[68] F.-Y. Su, C. You, Y.-B. He, W. Lv, W. Cui, F. Jin, B. Li, Q.-H. Yang, F. Kang, J. Mater. Chem. 20 (2010) 9644–9650.
[69] H. Li, C. Lu, B. Zhang, Electrochim. Acta 120 (2014) 96–101.
[70] X. Ma, G. Hou, Q. Ai, L. Zhang, P. Si, J. Feng, L. Ci, Sci. Rep. 7 (2017) 1–8.
[71] S. Wang, L. Shi, G. Chen, C. Ba, Z. Wang, J. Zhu, Y. Zhao, M. Zhang, S. Yuan, ACS Appl. Mater. Interfaces 9 (2017) 17163–17171.
[72] K. Chang, W. Chen, ACS Nano 5 (2011) 4720–4728.
[73] X. Wang, L. Fan, D. Gong, J. Zhu, Q. Zhang, B. Lu, Adv. Funct. Mater. 26 (7) (2016) 1104–1111.
[74] N. Liu, Z. Lu, J. Zhao, M.T. McDowell, H.W. Lee, W. Zhao, Y. Cui, Nat. Nanotechnol. 9 (2014) 187.
[75] Y. Xiao, J. Zai, X. Li, Y. Gong, B. Li, Q. Han, X. Qian, Nano Energy 6 (2014) 51–58.
[76] Y. Wang, S. Gai, N. Niu, F. He, P. Yang, J. Mater. Chem. A 1 (32) (2013) 9083–9091.
[77] Y. Huang, J. Luo, J. Peng, M. Shi, X. Li, X. Wang, B. Chang, J. Energy Storage 27 (2020) 101075.
[78] W.M. El Rouby, RSC Adv. 5 (82) (2015) 66767–66796.
[79] F. Bian, J. Yu, W. Song, H. Huang, C. Liang, Y. Gan, W. Zhang, Electrochim. Acta 330 (2020) 135248.
[80] S.E. Lee, H.J. Kim, H. Kim, J.H. Park, D.G. Choi, Nanoscale 5 (19) (2013) 8986–8991.
[81] X. Xie, P. Xiao, L. Pang, P. Zhou, Y. Li, J. Luo, Y. Li, J. Alloys Compd. 931 (2023) 167473.
[82] H.C. Tao, L.Z. Fan, Y. Mei, X. Qu, Electrochem. Commun. 13 (12) (2011) 1332–1335.
[83] J. Chang, X. Huang, G. Zhou, S. Cui, P.B. Hallac, J. Jiang, J. Chen, Adv. Mater. 26 (5) (2014) 758–764.
[84] M. Zhou, X. Li, B. Wang, Y. Zhang, J. Ning, Z. Xiao, L. Zhi, Nano Lett. *15* (9) (2015) 6222–6228.
[85] M. Zhao, D.L. Zhao, X.Y. Han, H.X. Yang, Y.J. Duan, X.M. Tian, Electrochim. Acta 287 (2018) 21–28.
[86] N. Jarulertwathana, V. Laokawee, W. Susingrat, S.J. Hwang, T. Sarakonsri, J. Mater. Sci. Mater. Electron. 28 (2017) 18994–19002.
[87] N. Mahmood, C. Zhang, F. Liu, J. Zhu, Y. Hou, ACS Nano 7 (11) (2013) 10307–10318.
[88] G. Huang, B. Cai, C. Zhan, P. Sun, Int. J. Electrochem. Sci 15 (2020) 5416–5429.
[89] E.H. Mohan, B.V. Sarada, R.V.R. Naidu, G. Salian, A.K. Haridas, B.A. Rao, T. N. Rao, Electrochimica Acta 219 (2016) 701–710.
[90] Q. Wang, C. Guo, Y. Zhu, J. He, H. Wang, Nano-Micro Lett. 10 (2018) 1–9.
[91] G. Huang, T. Chen, Z. Wang, K. Chang, W. Chen, J. Power Sources 235 (2013) 122–128.
[92] Li, X., Guo, Y., Li, Y., & Fu, R. Facile Synthesis of Co_3O_4@ G-C_3N_4 Available at SSRN 4193501.
[93] Li, X., Ma, Y., Qin, L., Zhang, Z., Zhang, Z., Zheng, Y. Z., & Qu, Y. (2015).
[94] Y. Li, Z. Wang, X.J. Lv, J. Mater. Chem. A 2 (37) (2014) 15473–15479.
[95] Sahu, T. S., Li, Q., Wu, J., Dravid, V. P., & Mitra, S. (2016).
[96] Xiaozhong, Z., Zhengfeng, Z., Xiaofang, L., Xueyan, L., Guofu, M., Qingtao, W., & Ziqiang, L. (2017).
[97] R. Chen, T. Zhao, W. Wu, F. Wu, L. Li, J. Qian, R. Xu, H. Wu, H.M. Albishri, A. S. Al-Bogami, D.A. El-Hady, J. Lu, K. Amine, Nano Lett. 14 (10) (2014) 5899–5904.
[98] J. Shi, Q. Ji, Z. Liu, Y. Zhang, Adv. Energy Mater. 28 (2016) 174–180.
[99] R. Zhang, J. Bao, Y. Pan, C.F. Sun, Chem. Sci. 10 (2019), 2604e2612.
[100] T.T. Debela, Y.R. Lim, H.W. Seo, I.S. Kwon, I.H. Kwak, J. Park, W.I. Cho, H. S. Kang, ACS Appl. Mater. Interfaces 10 (2018), 37928e37936.
[101] M.-H. Ryou, Y.M. Lee, K.Y. Cho, G.-B. Han, J.-N. Lee, D.J. Lee, et al., Electrochim. Acta 60 (2012) 23.
[102] H. Wang, S. Zhang, M. Zhu, G. Sui, X. Yang, J. Electroanal. Chem. 808 (2018) 303.
[103] X. Zeng, Z. Ding, C. Ma, L. Wu, J. Liu, L. Chen, D.G. Lvery, W. Wei, ACS Appl. Mater. Interfaces (2016), https://doi.org/10.1021/acsami.6b04770.
[104] D.H. Youn, C. Jo, J.Y. Kim, J. Lee, J.S. Lee, J. Power Sources 295 (2015) 228–234.
[105] S. Puravankara, P. Sharma, A. Kumar, S. Bankuru, J. Chakraborty, New J. Chem. (2020), https://doi.org/10.1039/C9NJ04662C.
[106] W. Lv, J. Xiang, F. Wen, Z. Jia, R. Yang, B. Xu, D. Yu, J. He, Z. Liu, Electrochim. Acta 153 (2015) 49–54.
[107] S. Liu, B. Shen, Y. Niu, M. Xu, Fabrication of WS2-nanoflowers@ rGO composite as an anode material for enhanced electrode performance in lithium-ion batteries,
J. Colloid Interface Sci. 488 (2017) 20–25.
[108] X. Xu, C.S. Rout, J. Yang, R. Cao, P. Oh, H.S. Shin, J. Cho, J. Mater, Chem. A 1 (2013) 14548–14554.
[109] Y. Du, X. Zhu, L. Si, Y. Li, X. Zhou, J. Bao, J. Phy, Chem. C 119 (2015) 15874–15881.

[110] D. Chen, G. Ji, B. Ding, Y. Ma, B. Qu, W. Chen, J.Y. Lee, Nanoscale 5 (2013) 7890–7896.
[111] H.T. Huu, H.T.T. Le, V.P. Nguyen, T.T.H. Nguyen, T.X.D. Nguyen, V.T. Nguyen, S. Kim, V. Vo, Electrochim. Acta 341 (2020) 136010.
[112] C. Feng, L. Huang, Z. Guo, H. Huakun Liu, Electrochem. Commun. 9 (2007) 119–122.
[113] K. Khan, M.B. Hanif, H. Xin, A. Hussain, H.G. Ali, B. Fu, Z. Fang, M. Motola, Z. Xu, M. Wu, Small (2023).
[114] J. Wan, Q. Chen, W. Li, L. Pan, Z. Zhao, D. Yu, Z. Tang, H. He, Electrochim. Acta 345 (2020) 136238.
[115] T.P. Nguyen, I.T. Il Tae Kim, Nanomaterials 10 (2020).
[116] T. Li, R. Ruisong Guo, Y. Luo, F. Li, L. Meng, X. Sun, Z. Yang, H. Luo, Y. Wan, Electrochim. Acta 331 (2020) (2020) 135424.
[117] ChemNanoMat https://doi.org/10.1002/cnma.201600188.
[118] Saima Batool, S., Idrees, M., Javed, M.J., Saleem, M., Kong, J. (2020). 246, (2020) 122832.
[119] ACS Appl. Mater. Interfaces 10 (2018) 37928–37936, https://doi.org/10.1021/acsami.8b10133.
[120] X.Q. Zhang, X.N. Li, J.W. Liang, Y.C. Zhu, Y.T. Qian, Small 12 (2016) 2484.
[121] C.T. Zhao, C. Yu, M.D. Zhang, Q. Sun, S.F. Li, M.N. Banis, X.T. Han, Q. Dong, J. Yang, G. Wang, Nano Energy 41 (2017) 66.
[122] J. Wang, J.L. Liu, D.L. Chao, J.X. Yan, J.Y. Lin, Z.X. Shen, Adv. Mater. 26 (2014) 7162.
[123] N. Feng, R.J. Meng, L.H. Zu, Y.T. Feng, C.X. Peng, J.M. Huang, G.L. Liu, B.J. Chen, J.H. Yang, Nat. Commun. 10 (2019) 1.
[124] Y.F. Li, Y.L. Liang, F.C.R. Hernandez, H.D. Yoo, Q.Y. An, Y. Yao, Nano Energy 15 (2015) 453.
[125] Z. Hu, L.X. Wang, K. Zhang, J.B. Wang, F.Y. Cheng, Z.L. Tao, J. Chen, Angew. Chem. Int. Ed. 53 (2014) 12794.
[126] Y. Zhang, T. He, G.L. Liu, L.H. Zu, J.H. Yang, Nanoscale 9 (2017) 10059.
[127] X. Zhang, R.F. Zhao, Q.H. Wu, W.L. Li, C. Shen, L.B. Ni, H. Yan, G. W. Angewandte Chemie International Edition, ACS Nano 11 (2017) 8429.
[128] Q. Yun, L. Li, Z. Hu, Q. Lu, B. Chen, H. Zhang, Adv. Mater. (2019) 1903826.
[129] J.G. Wang, H.Y. Liu, R. Zhou, X.R. Liu, B.Q. Wei, J. Power Sources 413 (2019) 327–333.
[130] X. Liu, Y. Wang, Y. Yang, W. Lv, G. Lian, D. Dmitri Golberg, X. Wang, X. Zhao, Y. Ding, Nano Energy 70 (2020) 104550.
[131] B. Qu, Y. Sun, L. Liu, C. Li, C. Yu, X. Zhang, Y. Chen, Sci. Rep. 7 (1) (2017) 42772.
[132] X. Chen, L. Li, S. Wang, C. Feng, Z. Guo, Mater. Lett. 164 (2016) 595–598.
[133] M.I.A. Abdel Maksoud, A.G. Bedir, M. Bekhit, M.M. Abouelela, R.A. Fahim, A. S. Awed, D.W. Rooney, Environ. Chem. Lett. 19 (2021) 3645–3681.
[134] J. He, Z. Jiao, MoS2/C3N, Appl. Surf. Sci. 580 (2022), 152371.
[135] Q. J. Peng, J. Zhou, Z. Sun, J. Phys. Chem. C 123 (18) (2019) 11493–11499.
[136] P. Xiang, X. Chen, J. Liu, B. Xiao, L. Yang, J. Phys. Chem. C 122 (17) (2018) 9302–9311.
[137] A. Samad, Y.H. Shin, ACS Appl. Mater. Interfaces 9 (35) (2017) 29942–29949.
[138] D. Cakir, C. Sevik, APS March Meeting Abstracts Vol. 2019, 2019, p. F47-010.
[139] H. Lin, N. Lou, D. Yang, R. Jin, Y. Huang, Janus MoSSe/graphene heterostructures: potential anodes for lithium-ion batteries, J. Alloys Compd. 854 (2021) 157215.
[140] Y. Li, W. Wu, F. Ma, Blue phosphorene/graphene heterostructure as a promising anode for lithium-ion batteries: a first-principles study with vibrational analysis techniques, J. Mater. Chem. A 7 (2) (2019) 611–620.
[141] Y. Wang, Z. Jiao, S. Ma, Y. Guo, Probing C3N/graphene heterostructures as anode materials for Li-ion batteries, J. Power Sources 413 (2019) 117–124.
[142] D. Cakir, C. Sevik, Tailoring storage capacity and ion kinetics in Ti2CO2/graphene heterostructures by functionalization of graphene, in: APS March Meeting Abstracts Vol. 2019, 2019, p. F47-010.
[143] K. Xu, N. Liao, M. Zhang, W. Xue, Nanoscale 12 (13) (2020) 7098–7108.
[144] G.C. Guo, D. Wang, X.L. Wei, Q. Zhang, H. Liu, W.M. Lau, L.M. Liu, J. Phys. Chem. Lett. 6 (24) (2015) 5002–5008.
[145] H. Lin, N. Lou, D. Yang, R. Jin, Y. Huang, J. Alloys Compd. 854 (2021) 157215.
[146] B. Guo, Y. Feng, X. Chen, B. Li, K. Yu, Appl. Surf. Sci. 434 (2018) 1021e1029.
[147] X. Zhang, R. Zhao, Q. Wu, W. Li, C. Shen, L. Ni, H. Yan, G. Diao, M. Chen, ACS Nano 11 (2017) 8429.
[148] Angew. Chem. Int. Ed. https://doi.org/10.1002/anie.202005840.
[149] Q.C. Pan, F.H. Zheng, Y.N. Wu, X. Ou, C.H. Yang, X.H. Xiong, M.L. Liu, J. Mater. Chem. A 6 (2018) 592–598.
[150] Q. Pan, F. Zheng, X. Ou, C. Yang, X. Xiong, M. Liu, Chem. Eng. J. 316 (2017) 393.
[151] Q. Pan, F. Zheng, X. Ou, C. Yang, X. Xiong, M. Liu, Chem. Eng. J. 316 (2017) 393–400.
[152] P. Hu, Z. Jia, Y. Wang, Q. Zhou, N. Liu, F. Li, J. Wang, ACS Appl, 2020 (Energy Mater).
[153] Chem. Eur. J. https://doi.org/10.1002/chem.201904085.
[154] P. Wang, H. Sun, Y. Ji, W. Li, X. Wang, Adv. Mater. 26 (2014) 964.
[155] W. Xu, T. Wang, Y. Yu, S. Wang, J. Alloy. Comp. 689 (2016) 460.
[156] S.B. Wang, B.Y. Guan, L. Yu, X.W. Lou, Adv. Mater. (2017) 29.
[157] Int. J. Electrochem. Sci., 15 (2020) 8171–8180.
[158] J. Zhang, Y. Li, T. Gao, X. Sun, Ceram. Int. 44 (2018) 8550.
[159] Nanoscale, 2020, 12, 1144.
[160] S. Kim, M. Hankel, W. Cha, G. Singh, J.M. Lee, I.Y. Kim, A. Ajayan Vinu, Nano Energy, 72 (2020) 104702, 2020.
[161] Y. Chen, B. Song, X. Tang, L. Lu, J. Xue, Small 10 (2014) 1536.
[162] K. Yang, T. Mei, Z. Chen, M. Xiong, X. Wang, J. Wang, J. Li, L. Yu, J. Qian, X. Wang, Nanoscale 12 (2020) 3435–3442.
[163] J. Dai, J. Li, Q. Zhang, M. Liao, T. Duan, W. Yao, Mater. Lett. 236 (2019) 483–486.
[164] T. Georgiou, R. Jalil, B. Belle, et al., Vertical feld-efect transistor based on graphene–WS_2 heterostructures for fexible and transparent electronics, Nat. Nanotechnol. 8 (2012) 100–103.
[165] S. Kim, K. Choi, B. Lee, et al., Rev. Mater. Res. 45 (2015) 63–84.
[166] M. Lukatskaya, O. Mashtalir, C. Ren, et al., Science 34 (2013) 1502–1505.
[167] Y. Li, Q. Zhang, T. Xu, et al., Ceram. Int. 44 (2018) 4058–4066.
[168] Q. Zhu, S. Zheng, X. Lu, et al., J. Alloys Compd. 654 (2016) 384–391.
[169] V. Davis, C.M. Bates, K. Omichi, et al., Science 362 (2018) 1144–1148.
[170] D. Arun Kumar, S. Selvasekarapandian, H. Nithya, et al., Mater. Chem. Phys. 143 (2014) 765–772.
[171] Q. Chen, Y. Wang, T. Zhang, et al., Electrochemical performance of LaF_3-coated LiMn2O4 cathode materials for lithium ion batteries, Electrochim. Acta 83 (2012) 65–72.
[172] M.W. Barsoum, M. Radovic, Annu. Rev. Mater. Res. 41 (2011) 195–227.
[173] Z.M. Sun, Int. Mater. Rev. 56 (2011) 143–166.
[174] J. Bao, L. Zhu, H. Wang, S. Han, Y. Jin, G. Zhao, Y. Zhu, X. Guo, J. Hou, H. Yin, J. Tian, J. Phys, Chem. C 122 (2018) 23329–23335.
[175] Q. Tang, Z. Zhou, P.J. Shen, Am. Chem. Soc. 134 (2012) 16909–16916.
[176] Y. Wang, Y. Li, Z. Qiu, X. Wu, P. Zhou, T. Zhou, J. Zhao, Z. Miao, J. Zhou, S. Zhuo, Fe3O4@Ti3C2 MXene hybrids with ultrahigh volumetric capacity as an anode material for lithium-ion batteries, J. Mater. Chem. A 6 (2018) 11189–11197.
[177] C. Zhang, S.-H. Park, A. Seral-Ascaso, S. Barwich, N. McEvoy, C.S. Boland, J. N. Coleman, Y. Gogotsi, V. Nicolosi, Nat. Commun. 10 (2019) 1–9.
[178] C. Chen, X. Xie, B. Anasori, A. Sarycheva, T. Makaryan, M. Zhao, Y. Gogotsi, Angewandte, Chemie International Edition 57 (7) (2018) 1846–1850.
[179] H. Aghamohammadi, R. Eslami-Farsani, E. Castillo-Martinez, J. Energy Storage 47 (2022) 103572.
[180] Q. Tang, Z. Zhou, P. Shen, J. Am. Chem. Soc. 134 (40) (2012) 16909–16916.
[181] J. Hu, B. Xu, C. Ouyang, Y. Zhang, S.A. Yang, RSC advances, 6(33), 27467–27474, 2016.
[182] S. Zhao, X. Meng, K. Zhu, F. Du, G. Chen, Y. Wei, Y. Gao, Energy Storage Mater. 8 (2017) 42–48.
[183] P. Barmann, R. Nölle, V. Siozios, M. Ruttert, O. Guillon, M. Winter, T. Placke, ACS Nano 15 (2) (2021) 3295–3308.
[184] J. Zhou, S. Lin, Y. Huang, P. Tong, B. Zhao, X. Zhu, Y. Sun, Chem. Eng. J. 373 (2019) 203–212.
[185] M. Naguib, R.R. Unocic, B.L. Armstrong, J. Nanda, Dalton Transactions, 44(20), 9353–9358, 2015.
[186] F. Du, H. Tang, L. Pan, T. Zhang, H. Lu, J. Xiong, J. Yang, C. (John) Zhang, Electrochim. Acta 235 (2017) 690.
[187] Z. Lin, D. Sun, Q. Huang, J. Yang, M.W. Barsoum, X. Yan, J. Mater. Chem. A 3 (2015) 14096.
[188] C. Shen, L. Wang, A. Zhou, B. Wang, X. Wang, W. Lian, Q. Hu, G. Qin, X. Liu, Nanomaterials 8 (2018) 80.
[189] Y. He, L. Wang, X. Wang, C. Shen, Q. Hu, A. Zhou, Liu, X, Materials in Electronics, Journal of Materials Science, 2020.
[190] F. Kong, X. He, Q. Liu, X. Qi, D. Sun, Y. Zheng, R. Wang, Y. Bai, Electrochem. commun. 97 (2018) 16.
[191] C. Zhang, S.-H. Park, A. Seral-Ascaso, S. Barwich, N. McEvoy, C.S. Boland, J. N. Coleman, Y. Gogotsi, V. Nicolosi, Nat. Commun. 10 (2019) 849.
[192] J. Phys, Chem. Lett. 10 (2019) 6446–6454.
[193] S. Zhao, X. Meng, K. Zhu, F. Du, G. Chen, Y. Wei, Y. Gogotsi, Y. Gao, Energy Storage Mater. 8 (2017) 42.
[194] C.F. Zhang, S.J. Kim, M. Ghidiu, M.Q. Zhao, M.W. Barsoum, V. Nicolosi, Y. Gogotsi, Adv. Funct. Mater. 26 (2016) 4143–4151.
[195] C. Zhang, S.J. Kim, M. Ghidiu, M.Q. Zhao, M.W. Barsoum, V. Nicolosi, Y. Gogotsi, Adv. Funct. Mater. 26 (2016) 4143.
[196] O. Mashtalir, M.R. Lukatskaya, M.Q. Zhao, M.W. Barsoum, Y. Gogotsi, Adv. Mater. 27 (2015) 3501.
[197] R. Liu, W. Cao, D. Han, Y. Mo, H. Zeng, H. Yang, W. Li, J. Alloys, Compd. 793 (2019) 505.
[198] Y. Wang, Y. Li, Z. Qiu, X. Wu, P. Zhou, T. Zhou, J. Zhao, Z. Miao, J. Zhou, S. Zhuo, J. Mater. Chem. A 6 (2018) 11189.
[199] J. Luo, X. Tao, J. Zhang, Y. Xia, H. Huang, L. Zhang, Y. Gan, C. Liang, W. Zhang, ACS Nano 10 (2016) 2491.
[200] M.-Q. Zhao, M. Torelli, C.E. Ren, M. Ghidiu, Z. Ling, B. Anasori, M.W. Barsoum, Y. Gogotsi, Nano Energy 30 (2016) 603.
[201] B. Anasori, Y. Xie, M. Beidaghi, J. Lu, B.C. Hosler, L. Hultman, P.R. Kent, Y. Gogotsi, M.W. Barsoum, ACS Nano 9 (2015) 9507.
[202] H. Liu, X. Zhang, Y. Zhu, B. Cao, Q. Zhu, P. Zhang, B. Xu, F. Wu, R. Chen, Nano-Micro Lett. 11 (2019) 65.
[203] B. Ahmed, D.H. Anjum, Y. Gogotsi, H.N. Alshareef, Nano Energy 34 (2017) 249–256.
[204] B. Ahmed, D.H. Anjum, Y. Gogotsi, H.N. Alshareef, Nano Energy 34 (2017) 249.
[205] Y. Zhang, Z. Mu, J. Lai, Y. Chao, Y. Yang, P. Zhou, Y. Li, W. Yang, Z. Xia, S. Guo, ACS Nano 13 (2019) 2167.
[206] B. Ahmed, D.H. Anjum, Y. Gogotsi, H.N. Alshareef, Nano Energy 34 (2017) 249.
[207] X. Wu, Z. Wang, M. Yu, L. Xiu, J. Qiu, Adv. Mater. 29 (2017) 1607017.
[208] X. Wu, Z. Wang, M. Yu, L. Xiu, J. Qiu, Adv. Mater. 29 (2017) 1607017.
[209] C. Chen, X. Xie, B. Anasori, A. Sarycheva, T. Makaryan, M. Zhao, P. Urbankowski, L. Miao, J. Jiang, Y. Gogotsi, Angew. Chem. Int. Ed. 57 (2018) 1846.
[210] J. Halim, S. Kota, M.R. Lukatskaya, M. Naguib, M.Q. Zhao, E.J. Moon, J. Pitock, J. Nanda, S.J. May, Y. Gogotsi, M.W. Barsoum, Adv. Funct. Mater. 26 (2016) 3118.

[211] X. Sun, Y. Liu, J. Zhang, L. Hou, J. Sun, C. Yuan, Electrochim. Acta 295 (2019) 237.
[212] F. Wang, Z.J. Wang, J.F. Zhu, H.B. Yang, X.J. Chen, L. Wang, C.H. Yang, J. Mater. Sci. 52 (2017) 3556–3565.
[213] Y.T. Liu, P. Zhang, N. Sun, B. Anasori, Q.Z. Zhu, H. Liu, Y. Gogotsi, B. Xu, Adv. Mater. 30 (2018) 1707334.
[214] F. Wang, Z. Wang, J. Zhu, H. Yang, X. Chen, L. Wang, C. Yang, J. Mater. Sci. 52 (2017) 3556.
[215] G. Zou, Z. Zhang, J. Guo, B. Liu, Q. Zhang, C. Fernandez, Q. Peng, ACS Appl. Mater. Interfaces 8 (2016) 22280.
[216] G. Zou, Z. Zhang, J. Guo, B. Liu, Q. Zhang, C. Fernandez, Q. Peng, ACS Appl. Mater. Interfaces (2016) 8,22280.
[217] P. Zhang, D. Wang, Q. Zhu, N. Sun, F. Fu, B. Xu, Nano-Micro Lett. 11 (2019) 81.
[218] B. Ahmed, D.H. Anjum, M.N. Hedhili, Y. Gogotsi, H.N. Alshareef, Nanoscale 8 (2016) 7580.
[219] Y.T. Liu, P. Zhang, N. Sun, B. Anasori, Q.Z. Zhu, H. Liu, Y. Gogotsi, B. Xu, Adv. Mater. 30 (2018) 1707334.
[220] C. Yang, Y. Liu, X. Sun, Y. Zhang, L. Hou, Q. Zhang, C. Yuan, Electrochim. Acta 271 (2018) 165.
[221] J. Huang, R. Meng, L. Zu, Z. Wang, N. Feng, Z. Yang, Y. Yu, J. Yang, Nano Energy 46 (2018) 20.
[222] R. Meng, J. Huang, Y. Feng, L. Zu, C. Peng, L. Zheng, L. Zheng, Z. Chen, G. Liu, B. Chen, Y. Mi, J. Yang, Adv. Energy Mater. 8 (2018) 1801514.
[223] C. Wei, H. Fei, Y. An, Y. Zhang, J. Feng, Electrochim. Acta 309 (2019) 362.
[224] J. Wang, S. Dong, H. Li, Z. Chen, S. Jiang, L. Wu, X. Zhang, J. Electroanal. Chem. 810 (2018) 27.
[225] Y. Tao, et al., Few-layer phosphorene: an emerging electrode material for electrochemical energy storage, Appl. Mater. Today 15 (2019) 18–33.
[226] L. Cartz, S. Srinivasa, R. Riedner, J. Jorgensen, T. Worlton, J. Chem. Phys. 71 (1979) 1718–1721 [437]. J. Slater, G. Koster, J. Wood, Phys. Rev., 126 (1962) 1307.
[227] M. Baba, Y. Nakamura, Y. Takeda, K. Shibata, A. Morita, Y. Koike, T. Fukase, J. Phys, Condens. Matter 4 (1992) 1535–1544.
[228] S. Narita, Y. Akahama, Y. Tsukiyama, K. Muro, S. Mori, S. Endo, M. Taniguchi, M. Seki, S. Suga, A. Mikuni, Phys. B C 117 (1983) 422–424.
[229] J. Qiao, X. Kong, Z.-X. Hu, F. Yang, W. Ji, Nat. Commun. 5 (2014) 4475.
[230] V.V. Kulish, O.I. Malyi, C. Persson, P. Wu, Phys. Chem. Chem. Phys. 17 (2015) 13921–13928.
[231] Q. Jiang, J. Li, N. Yuan, Z. Wu, J. Tang, Electrochim. Acta 263 (2018) 272–276.
[232] Y. Zhao, S. Zeng, J. Ni, Phys. Rev. B 93 (1) (2016) 14502.
[233] J.ur Rehman, M.H. Chowdhury, IEEE International Conference on Flexible and Printable Sensors and Systems (FLEPS), 2019, pp. 1–3.
[234] G.L. Pearson, J. Bardeen, Phys. Rev. 75 (5) (1949) 865.
[235] T.-T. Yu, P.-F. Gao, Y. Zhang, S.-L. Zhang, Appl. Surf. Sci. 486 (2019) 281–286.
[236] A.G. Dylla, P. Xiao, G. Henkelman, K.J. Stevenson, J. Phys. Chem. Lett. 3 (2012), 2015 2019.
[237] S. Liu, H. Jia, L. Han, J. Wang, P. Gao, D. Xu, J. Yang, S. Che, Adv. Mater. 24 (2012) 3201–3204.
[238] A.G. Dylla, G. Henkelman, K.J. Stevenson, Acc. Chem. Res. 46 (2013) 1104–1112.
[239] J.ur Rehman, M.H. Chowdhury, IEEE International Conference on Flexible and Printable Sensors and Systems (FLEPS), 2019, pp. 1–2.
[240] N.K. Jena, R.B. Araujo, V. Shukla, R. Ahuja, ACS Appl. Mater. Interfaces 9 (2017) 16148.
[241] Jingzhen Li, et al., J. Electrochem. Soc. 167 (2020), 090527.
[242] C. Zhu, C. Wen, C. Wang, M. Zhang, Y. Geng, Z. Su, J. Mater. Chem. A 9 (17) (2021) 10855–10868.
[243] D.W. Rao, L.Y. Zhang, Z.S. Meng, X.R. Zhang, Y.H. Yang, G.J. Qiao, X.Q. Shen, H. Xia, J.H. Liu, R.F. Lu, J. Mater, Chem. A 5 (2017) 2328–2338.
[244] D. Ayodhya, G. Veerabhadram, A brief review on synthesis, properties and lithium-ion battery applications of borophene, FlatChem 19 (2020) 100150.
[245] C. Zhang, M. Yu, G. Anderson, R.R. Dharmasena, G. Sumanasekera, Nanotechnology 28 (2017), 075401.
[246] Y. Zhang, H. Wang, Z. Luo, H.T. Tan, B. Li, S. Sun, Z. Li, Y. Zong, Z.J. Xu, Y. Yang, K.A. Khor, Q. Yan, Adv. Energy Mater. 6 (2016) 1600453.
[247] Y. Li, W. Wu, F. Ma, J. Mater, Chem. A 7 (2019) 611–620.
[248] Q. Peng, Z. Wang, B. Sa, B. Wu, Z. Sun, ACS Appl. Mater. Interfaces 8 (2016) 13449–13457.
[249] J. Bao, L. Zhu, H. Wang, S. Han, Y. Jin, G. Zhao, Y. Zhu, X. Guo, J. Hou, H. Yin, J. Tian, J. Phys, Chem. C 122 (2018) 23329–23335.
[250] Sensors 18 (11) (2018) 3638.
[251] H. Liu, A.T. Neal, Z. Zhu, et al., ACS Nano 8 (2014) 4033–4041.
[252] N.O. Weiss, H. Zhaou, L. Liao, et al., Adv. Mater. 24 (2012) 5782–5825.
[253] Hongwei Z. Academic Press: Cambridge, MS, USA.
[254] Le Shi, Tianshou Zhao, J. Mater. Chem. A 5 (8) (2017) 3735–3758.
[255] S.H. Yu, M.J. Zachman, K. Kang, H. Gao, X. Huang, F.J. DiSalvo, J. Park, L. F. Kourkoutis, H.D. Abruña, Adv. Energy Mater. 9 (2019) 1902773.
[256] L. Zhang, D. Sun, J. Kang, J. Feng, H.A. Bechtel, L.-W. Wang, E.J. Cairns, J. Guo, Nano Lett. 18 (2018) 1466.
[257] ChemSusChem https://doi.org/10.1002/cssc.201902706.
[258] C.J. Fu, G.G. Zhao, H.J. Zhang, S. Li, Int. J. Electrochem. Sci. 8 (2013) 6269.
[259] C. Liu, X.G. Liu, J. Tan, Q.F. Wang, H. Wen, C.H. Zhang, J. Power Sources 342 (2017) 157.
[260] C. Zhong, J.Z. Wang, D. Wexler, H.K. Liu, Carbon 66 (2014) 637.
[261] R.P. Zhang, Y. Wang, M.Q. Jia, J.J. Xu, E. Pan, Appl. Surf. Sci. 437 (2017) 375.
[262] Huijuan Cui, Yibo Guo, Wei Ma, Zhen Zhou, ChemSusChem 13 (6) (2020) 1155–1171.